PASJ: Publ. Astron. Soc. Japan , 1–??,
© 2008. Astronomical Society of Japan.

arXiv:astro-ph/0407419v1 20 Jul 2004

SiO Maser Survey of IRAS Sources in the Inner Galactic Disk

Shuji Deguchi[1], Takahiro Fujii[2,3], Ian S. Glass[4], Hiroshi Imai[2,3,5], Yoshifusa Ita[6], Hideyuki Izumiura[7], Osamu Kameya[2,8], Atsushi Miyazaki[1], Yoshikazu Nakada[6] and Jun-ichi Nakashima[9,10]

[1] *Nobeyama Radio Observatory, National Astronomical Observatory, Minamimaki, Minamisaku, Nagano 384-1305*

[2] *VERA Project Office, National Astronomical Observatory, 2-21-1 Osawa, Mitaka, Tokyo 181-8588*

[3] *Faculty of Science, Kagoshima University, 1-21-35 Korimoto, Kagoshima 890-0065*

[4] *South African Astronomical Observatory, PO Box 9, Observatory 7935, South Africa*

[5] *Joint Institute for VLBI in Europe, Postbus 2, 7990 AA Dwingeloo, The Netherlands*

[6] *Institute of Astronomy, School of Science, The University of Tokyo, 2-21-1 Osawa, Mitaka, Tokyo 181-0015*

[7] *Okayama Astrophysical Observatory, National Astronomical Observatory, Kamogata, Asakuchi, Okayama 719-0232*

[8] *Mizusawa Astrogeodynamics Observatory, National Astronomical Observatory, Mizusawa, Iwate 023-0861*

[9] *Department of Astronomical Science, The Graduate University for Advanced Studies, Minamimaki, Minamisaku, Nagano 384-1305*

[10] *Department of Astronomy, University of Illinois at Urbana-Champaign 1002 W. Green St. , Urbana, IL 61801, U.S.A.*

(PASJ — 2004 Aug. 25 issue in press)

(Received 2004 May 6; accepted 2004 July 9)

Abstract

We have surveyed 401 color selected IRAS sources in the Galactic disk in the SiO $J = 1$–0 $v = 1$ and 2 maser lines at 43 GHz, resulting in 254 (239 new) detections. The observed sources lie mostly in a strip of the inner Galactic disk with boundaries $-10^\circ < l < 40^\circ$ and $|b| < 3^\circ$. This survey provides radial velocities of inner-disk stars for which optical measurements cannot be made due to interstellar extinction. The SiO l–v diagram in the area $-10^\circ < l < 40^\circ$ exhibits fewer objects coincident with the molecular ring feature than the OH 1612 MHz source l–v map does, indicating a slight difference of stellar type between SiO and OH emitting stars. After identifying all of the SiO detected sources in the 2MASS near-infrared catalog, we computed their luminosity distances based on the infrared fluxes. We then mapped these objects onto the first quadrant of the Galactic plane. Combining the distances with the SiO radial-velocities, we obtained a pattern speed for SiO maser sources, $\Omega_{\rm P} = 21\ (\pm 13)$ km s^{-1} kpc^{-1}, between the distances 1 and 5.5 kpc, without the use of any dynamical models. The increase of the pattern speed toward the Galactic center (up to 60 km s^{-1} kpc^{-1} between the distances, 5.5 and 7 kpc) suggests the presence of two pattern speeds in the Galaxy.

Key words: Galaxy: disk, kinematics and dynamics — masers — stars: AGB and post-AGB

1. Introduction

Observations of OH 1612 MHz and SiO maser sources (te Lintel-Hekkert et al. 1991; Jiang et al. 1996; Sevenster et al. 1997) provide basic radial velocity data for stars throughout the Galaxy with an accuracy of a few km s^{-1}. The accumulation of radial-velocity data is useful for studying the rotation of the inner and outer parts of the Galaxy (Nakashima et al. 2000(; Nakashima, Deguchi 2003a), and complements the radial-velocity data based on the HI and CO gas. At visible wavelengths, these data are difficult to obtain because of interstellar extinction in the Galactic disk. In particular, the radial velocity data can be used to obtain the pattern speed of the Galaxy without appealing to dynamical models (Debattista et al. 2002).

The SiO masers arise mostly in the circumstellar envelopes of mass-losing evolved stars in the Asymptotic Giant Branch (AGB) phase (or occasionally the post-AGB phase), which are intrinsically bright in the near- and mid-infrared regions. Though many surveys have been made during the last decade in SiO and OH, a considerable number of candidate stars for masers in the inner part of the Galactic disk have not previously been observed. The present paper aims to improve the radial velocity data in the sky areas where the maser surveys have been relatively poor.

Though a large number of OH 1612 MHz objects have been detected in the area $|l| < 45^\circ$ and $|b| < 3^\circ$ (Sevenster et al. 2001), SiO maser sources have not been the sub-

ject of deep searches [except for Izumiura et al. (1999), and Deguchi et al. (2000b) who looked at objects having a relatively narrow infrared color range]. A comparison of variables detected in SiO with those detected in OH 1612 MHz at the Galactic center (Imai et al. 2002; Deguchi et al. 2004) revealed that OH 1612 MHz objects tend to be of longer period than those detected in SiO; in the period range between 200–500 days, the detection rate of SiO is triple that of OH. This fact indicates that the SiO maser samples are weighted towards stars with smaller mass than the OH maser samples, based on the observed increase of mass with period for Miras (e.g., Feast 1996). In addition, the OH 1612 MHz sample always involves some contamination by young objects associated with star forming regions (SFR), and therefore molecular clouds, even though they have doubly peaked line profiles (Caswell 1999). These might bias the radial-velocity statistics to some degree because Galactic gas dynamics are considerably different from stellar dynamics (see, for example, Binney et al. 1991). In this sense, the SiO maser radial-velocity sample can rectify such a bend for studying Galactic dynamics. Furthermore, in previous surveys (for example, Nakashima, Deguchi 2003a), the overlap of objects with SiO and OH 1612 MHz was only 1/3 of the detected objects. Therefore, it is useful to increase the number of SiO detections to enlarge the sample.

Apart from the fact that SiO maser observations of color-selected IRAS sources provide basic data on radial velocities, they show with certainty that these objects are O-rich mass-losing evolved stars. Though classifications of IRAS point sources have been made using IRAS low resolution spectra and IRAS colors (Kwok et al. 1997), the natures of some of the faint objects with red IRAS colors remain uncertain, i.e., as to whether they are evolved (AGB/post AGB) stars or young stellar objects. IRAS colors or even IRAS low resolution spectra (LRS) can often be insufficient for this purpose (for example, LRS class=1n or 3n objects; Olnon et al. 1986).

In this paper, we present the survey data with minimum interpretation. We have now accumulated a large amount of SiO data (403 objects during the past 8 years of observations); some objects have turned out to be quite interesting. About 85 percent of the objects in the present paper are in the area $-10^\circ < l < 40^\circ$ and $|b| < 3^\circ$ because the surveys were made as a backup program during two other long-term projects looking towards the Galactic center.

2. Observations

Simultaneous observations in the SiO $J = 1$–0, $v = 1$ and 2 transitions at 42.122 and 42.821 GHz, respectively, were made with the 45-m radio telescope at Nobeyama during the period 1997 January–2003 May. We used a cooled SIS mixer receiver (S40) for the 43 GHz observations and accousto-optical spectrometer arrays, AOS-H and AOS-W, having bandwidths of 40 and 250 MHz. The effective velocity resolution of the AOS-H spectrometer is 0.3 km s^{-1}. They cover the velocity range of $\pm$350 km s^{-1}, for both the SiO $J = 1$–0 $v = 1$ and 2 transitions, simultaneously. The overall system temperature was between 200 and 300 K, depending on weather conditions. The half-power telescope beam width (HPBW) is about $40''$. The antenna temperature (T_a) given in the present paper is that corrected for the atmospheric and telescope ohmic loss but not for the beam or aperture efficiency. The conversion factor of the antenna temperature to the flux density is approximately 2.9 Jy K^{-1}. We employed the position switching mode. Further details of SiO maser observations using the NRO 45-m telescope have been described elsewhere (Deguchi et al. 2000a), and are not repeated here.

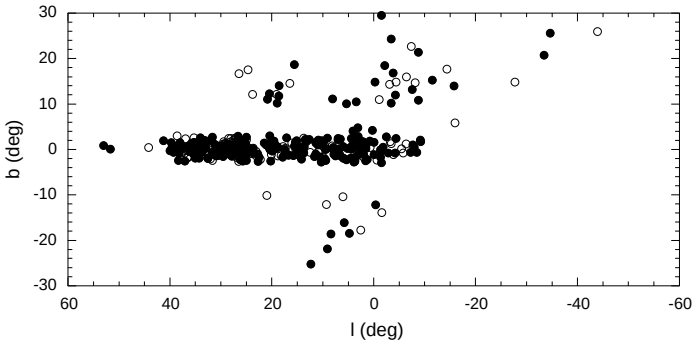

Fig. 1. Source distribution in Galactic coordinates. Filled and unfilled circles indicate SiO detections and nondetections.

The sources observed in this paper were mainly selected according to the following criteria:

1. IRAS sources in the narrow color range, $0.0 < C_{12} (= log(F_{25}/F_{12}) < 0.1$, in the area, $25^\circ < l < 40^\circ$ and $|b| < 3^\circ$, where F_{12} and F_{25} are the IRAS flux densities at 12 and 25 μm. The surveys of these sources were made during the 1997–1999 long-term observations of IRAS sources in the Galactic disk (Izumiura et al. 1999).
2. The IRAS sources in the color ranges, $-0.1 < C_{12} < 0.0$ and $0.1 < C_{12} < 0.2$, in the area, $-10^\circ < l < 40^\circ$ and $|b| < 3^\circ$. These sources were observed in the 2001–2003 winter–spring seasons during the long-term SiO maser survey of large-amplitude variables in the Galactic center (Imai et al. 2002). The observed positions were the MSX_5CG source positions (Egan et al. 1999) within $20''$ of IRAS sources, but were selected according to their IRAS colors for consistency with the previous surveys.

The criteria that were used after 2000 effectively exclude some young stellar objects in dust clouds; they are very often clustered and the MSX images frequently resolve those for which the IRAS catalog gives only a single strong source. Furthermore, the later-half survey after 2000 was limited to relatively bright objects ($F_{12} \gtrsim 5$ Jy).

In addition, from time to time, we observed objects at higher galactic latitudes ($|b| > 10^\circ$) where the surveys were formerly incomplete. These sources were mostly observed

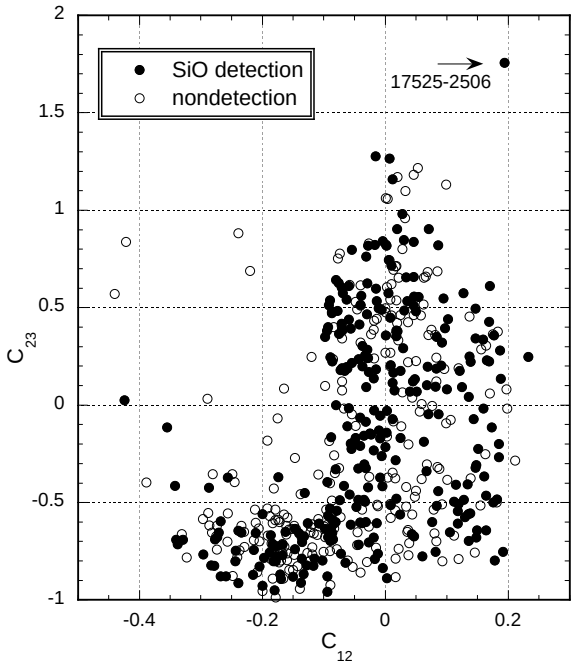

Fig. 2. IRAS two-color diagram of the observed sources. Filled and unfilled circles indicate the SiO detections and nondetections. IRAS 17525-2506 shows extreme colors as an AGB star (see text). Two other objects, 16342−3814 and 18596+0315, have extreme colors and are outside this figure.

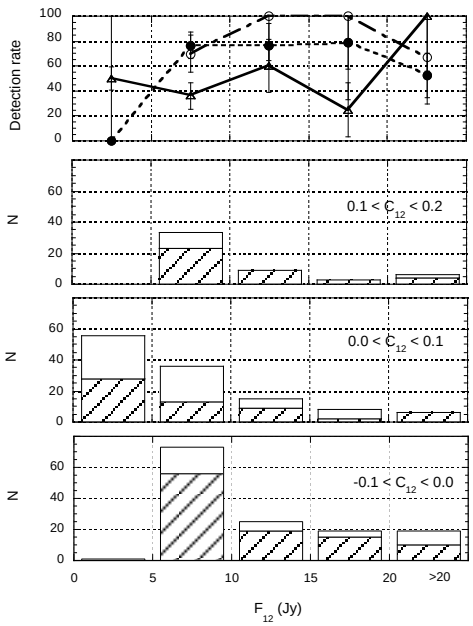

Fig. 3. Detection probability (top line graph) and histograms of flux density (lower three). The broken, solid, and dash-dot lines in the top line graph indicate the subsamples of objects with $-0.1 < C_{12} < 0.0$, $0.0 < C_{12} < 0.1$, and $0.1 < C_{12} < 0.2$, respectively. The shaded and unshaded histograms indicate the SiO detection and nondetection, respectively. The detection rate for objects with $0.0 < C_{12} < 0.1$ appears to be lower than that for objects with other colors, but this is an observational selection effect (see main text).

as backups during poor weather conditions, such as when strong wind or thick cloud hindered sensitive observations. Several low declination sources ($\delta \lesssim -30°$) were also observed during conditions when a part of the antenna surface was covered with ice (but the weather was mostly clear). On such occasions, we could observe bright objects at very low elevation angles, which were normally not considered suitable.

In total, we observed 401 IRAS sources and detected 254 in the SiO $J = 1$–0 $v = 1$ or 2 transitions in the sky area $-60° < l < 60°$. The results are summarized in tables 1 and 2 for 254 detections and 147 nondetections, respectively. Previous OH/SiO observations are noted in the last two columns of table 1 as "y" (detection) and "n" (nondetection), with references. Among 254 detected sources, 239 are new SiO detections, and 183 were not detected before in either OH 1612 MHz or SiO maser lines. The distribution of the observed objects in Galactic coordinates is shown in figure 1. As seen in this figure, about 85% of the objects (342 sources) were in the area $-10° < l < 40°$ and $|b| < 3°$. Of these, 216 are SiO detections, giving a detection rate of 63 %. Discussions of individual objects and the spectra of SiO detections are given in the Appendix.

Figure 2 shows the two-color diagram of the observed sources. In this figure, we see a sudden decrease of objects at $C_{12} < -0.1$. However, this is totally an observational selection effect, because the color-selection criteria were slightly different for the high galactic latitude stars ($|b| > 3°$) (because contamination to the IRAS 60 μm flux density by molecular clouds is negligible at the high latitudes; see Izumiura et al. (1999)), In the Galactic disk area, $l < 40°$ and $|b| < 3°$, contamination of the IRAS 60 μm flux density by dust clouds causes an increase of SiO detectable objects at $C_{23} > 0$, which is a region not populated by AGB stars (van der Veen, Habing 1988). This is well known and discussed in various papers (Izumiura et al. 1999).

Figure 3 shows a comparison of SiO detection rates in the subsamples of the color ranges, $-0.1 < C_{12} < 0.0$, $0.0 < C_{12} < 0.1$, and $0.1 < C_{12} < 0.2$. Apparently, the detection rate for objects in the color range $0.0 < C_{12} < 0.1$ is lower than the detection rates for objects in the other color ranges. However, this is due to a selection bias in the sources that were observed (The objects in IRAS color range $0.0 < C_{12} < 0.1$ were selected and observed before 2000, when the MSX catalog was not available, while those in the IRAS color ranges, $-0.1 < C_{12} < 0.0$

and $0.1 < C_{12} < 0.2$ were selected after 2000, making use of the MSX catalog). The positional accuracies of the MSX sources ($\sim 3''$) were much improved over those of the IRAS Point Source catalog ($\sim 10''$). Furthermore, the known young stellar objects are excluded (using the SIMBAD database, MSX images, and 2MASS images) in the observations after 2000. Thus, because of the improvements in the source selection and positions, we have SiO detection rates as high as ~ 80 % for the objects in the range $-0.1 < C_{12} < 0.0$ and $0.1 < C_{12} < 0.2$.

3. Discussion

Note that the present SiO survey was made with pointed observations and is not an unbiased survey as is the case with the OH 1612 MHz survey (Sevenster et al. 2001). A possible bias in the detection rate may be caused by the source selection process using two different catalogs (IRAS and MSX), as noted in the previous section. Nevertheless, the present SiO maser sample is large enough as a basic database of radial velocities of evolved stars in the inner Galactic disk. With the above caution in mind, we discuss the radial velocity data.

3.1. l-v diagram

The left panel of figure 4 shows a longitude–velocity diagram for the SiO detected sources in this paper (open circles). For the purpose of comparing this figure with the OH l–v diagram (right panel), we added 277 SiO detected sources (squares) within the color range, $0.0 < C_{12} < 0.1$, in $-10^\circ < l < 25^\circ$ and $|b| < 3^\circ$ from previous papers (Izumiura et al. 1999; ; Deguchi et al. 2000a; Deguchi et al. 2000b). The addition makes the total number of SiO detections 493, similar to the total number of OH 1612 MHz detections (583 in the same region). The l–v diagrams are overlaid on the CO $J = 1$–0 map (Dame et al. 2001), which gives an approximate idea of the range of velocities due to the Galactic rotation.

The overall patterns in the SiO and OH l–v diagrams resemble each other: the SiO l–v map (figure 4) exhibits two areas with no detections which are indicated as ellipses H1 and H2. The same empty regions can also be seen in the OH l–v diagram (the right panel of figure 4) [also in the 86GHz SiO l–v diagram of Messineo et al. (2002)]. The presence of such vacant regions in the l–v diagram seems to indicate that a spatial density of IRAS sources is considerably low in inter-arm regions (for H1), and also irregular even in spiral arms (for H2), though the IRAS source density, when integrated on the line of sight, does not vary much along longitude.

Furthermore, we can recognize subtle differences between the two panels; the SiO sources seem to avoid the 3 kpc arm feature, which is shown as the broken line in the left panel of figure 4, but this void does not seem to appear strongly in the OH map (right panel). In addition, the OH distribution seems to correlate strongly with the molecular ring feature which extends approximately between (l,$V_{\rm lsr}$)=(10°, 20 km s^{-1}) and (25°, 60 km s^{-1}). However, the SiO map does not seem to show such a very strong concentration towards the molecular ring. Rather, it shows a high concentration of sources near the upper edge of the molecular ring feature at (l,$V_{\rm lsr}$) $\sim$(19°, 70 km s^{-1}). This impression, i.e., that there is less concentration of SiO sources towards the molecular ring, comes mainly from the sparse distribution of SiO detections around (l,$V_{\rm lsr}$) $\sim(17 \pm 1.25^\circ$, 35$\pm$25 km s^{-1}), whereas the OH l–v diagram exhibits a high density of detections at the same region. However, it turns out that the impression is not correct; we count, in fact, the SiO sources, 18204−1344 (=IRC −10414), and the other three (18162−1422, 18182−1447, and 18187−1430, detected by SiO in Messineo et al. (2002)) falling in this spatial and velocity range. These are simply dropped from the present survey list due to color-selection criteria, and not shown in figure 4.

The filled triangles in the OH l–v diagram (the right panel in figure 4) indicates OH 1612 MHz double-peak sources without NIR counterparts within $5''$ of their positions. More than half of these objects are considered to be gas clouds in star forming regions (not evolved stars), which often emit dominant OH 1665 MHz masers (of course, not all of them necessarily follow this rule ; Caswell 1999). We can see that these filled triangles (SFR candidates) are concentrated strongly along the molecular ring feature in the right panel of figure 4 (and with the nuclear disk, which is in the range $|l| \lesssim 1^\circ$ and $|V_{\rm lsr}| \lesssim 200$ km s^{-1}).

The sample of OH 1612 MHz sources with doubly peaked spectra involves a variety of objects: AGB and post-AGB stars, planetary nebulae as well as gas clouds in star forming regions (Caswell 1999). On the other hand, the SiO sample involves purely AGB stars (very few post-AGB and young stellar objects). It is well known that the gas dynamics differs considerably from the stellar dynamics in the Galaxy (e.g., Binney et al. 1991). Counting the OH 1612 MHz objects without NIR counterparts in the 2MASS database, we estimate that more than 10 % of the Sevenster et al. (1997)'s OH 1612 MHz objects are likely to be gas clouds in SFRs (of course, the percentage is somewhat uncertain, depending on the color selection criteria and the limiting magnitudes in the NIR bands).

Therefore, we concluded that the OH and SiO surveys are looking at slightly different (stellar) types of stars. Especially, exclusion of SFR OH 1612 MHz sources from the OH sample is crucial when making comparisons between the OH and SiO samples.

3.2. 2MASS identifications of IRAS sources and estimation of distances

Identifications of IRAS sources with 2MASS near-infrared objects were made in terms of $H-K$ colors and K magnitudes (see detail in Deguchi et al. 1998). Table 4 gives a summary of the identifications of the IRAS sources with SiO detections, listing IRAS name, MSX 5CG name, right ascension and declination in J2000, J, H, and K magnitudes, blending flag, and the distance from the Sun. Near-infrared identifications of the IRAS sources were made successfully for all the objects except

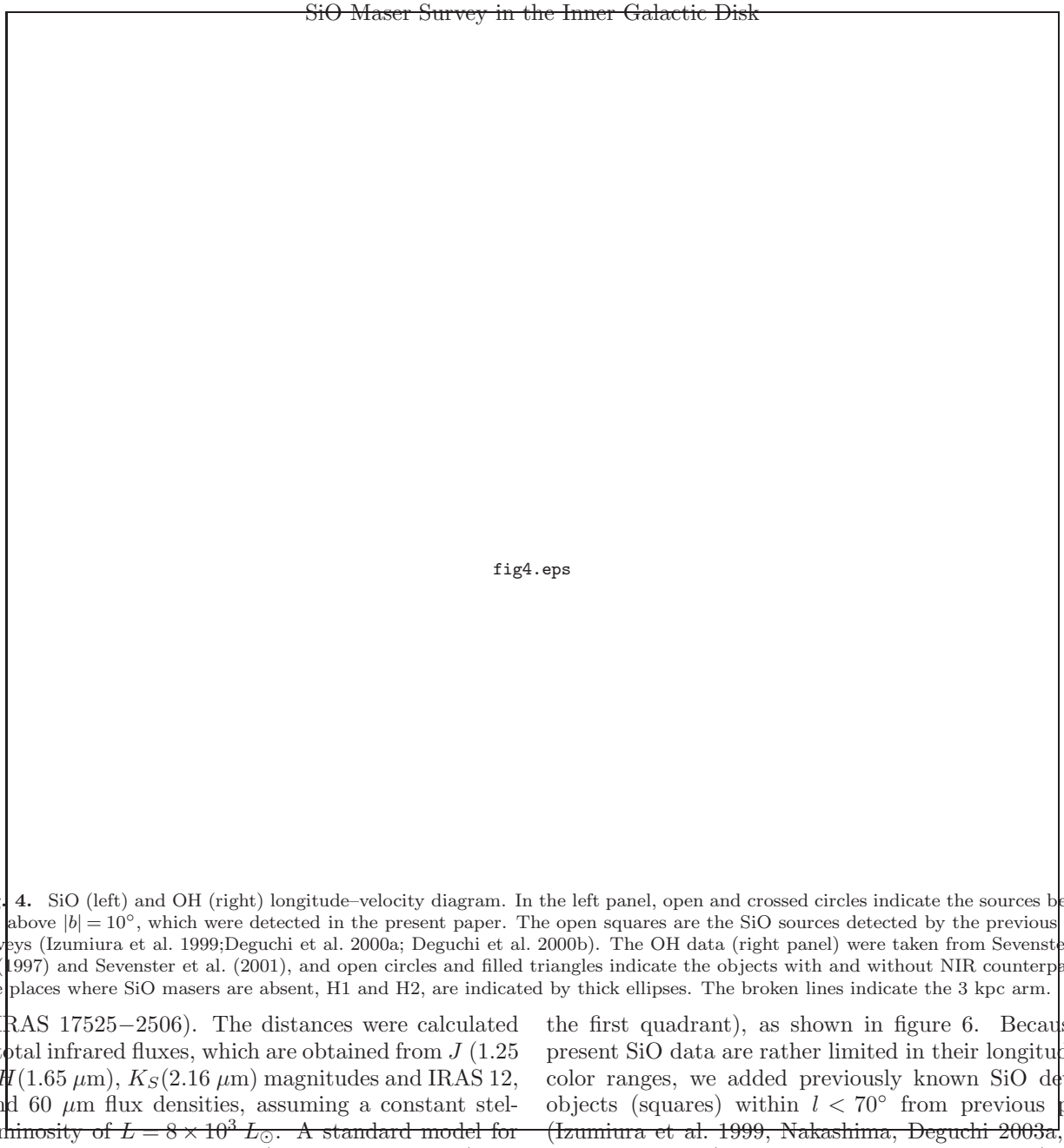

Fig. 4. SiO (left) and OH (right) longitude–velocity diagram. In the left panel, open and crossed circles indicate the sources below and above $|b| = 10^\circ$, which were detected in the present paper. The open squares are the SiO sources detected by the previous SiO surveys (Izumiura et al. 1999;Deguchi et al. 2000a; Deguchi et al. 2000b). The OH data (right panel) were taken from Sevenster et al. (1997) and Sevenster et al. (2001), and open circles and filled triangles indicate the objects with and without NIR counterparts. The places where SiO masers are absent, H1 and H2, are indicated by thick ellipses. The broken lines indicate the 3 kpc arm.

one (IRAS 17525−2506). The distances were calculated from total infrared fluxes, which are obtained from J (1.25 μm), H(1.65 μm), K_S(2.16 μm) magnitudes and IRAS 12, 25, and 60 μm flux densities, assuming a constant stellar luminosity of $L = 8 \times 10^3\ L_\odot$. A standard model for the dust extinction distribution (Unavane et al. 1998) was used to get the extinction correction in the galactic disk [see Deguchi et al. (1998) in detail]. Plots of $J-K$ and K against $H-K$ of the identified objects are shown in figure 5, where the broken lines in the left and right panels indicate the expected $J-H$ and K magnitude variations due to interstellar and circumstellar extinction, respectively. The squares in the lower-left indicate the position of an M6 III star without extinction (at a distance of 8 kpc in the right panel). In the left panel, most of the points (except stars with low photometric quality which are indicated with open triangles) fall near the broken line as expected. In the right panel, most of points fell below the broken line, suggesting that the distances of these stars are smaller than 8 kpc.

Using the distances that we obtained, we mapped the positions of the SiO detections on the galactic plane (in the first quadrant), as shown in figure 6. Because the present SiO data are rather limited in their longitude and color ranges, we added previously known SiO detected objects (squares) within $l < 70^\circ$ from previous papers (Izumiura et al. 1999, Nakashima, Deguchi 2003a, etc.). A spiral model (figure 1 of Taylor, Cordes 1993), which indicates spiral arms and HII regions, was overlaid on the figure. We can recognize large concentrations of sources, one in the area around (3, 0.5) and the other near the line connecting the points (5, 3) and (0, 8). The latter concentration of sources corresponds to the Bulge bar, and has been discussed previously (for example, Dwek et al. 1995; Nikolaev, Weinberg 1997); this feature was already recognizable in the smaller sample of narrow C_{12} color range objects (see figure 6 of Deguchi et al. 2002). The other concentration of sources, around (3, 0.5), is located near a dense area of HII regions, corresponding to the "molecular ring feature" in the l–v diagram (Dame et al. 2001). Note that no large concentration was found towards the "3 kpc ring" feature except for the starting point of the feature around (4.8, 1), which corresponds to the tip of the Bulge bar.

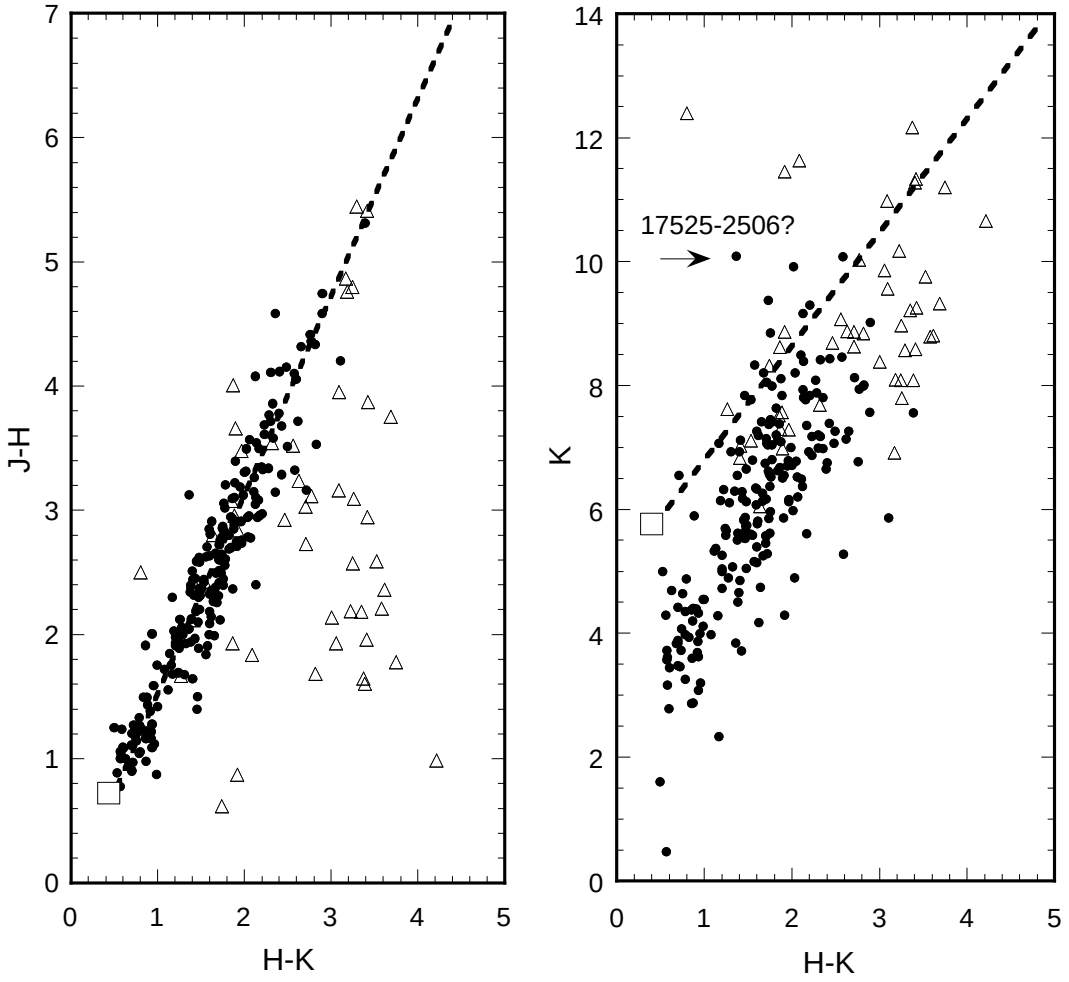

Fig. 5. Plots of $J-H$ (left panel) and K (right panel) against $H-K$ for the 2MASS identified stars. Filled circles and open triangles indicate the objects with high and low photometric qualities, respectively. The squares in the lower-left indicates the position of a M6 III star without extinction (at a distance of 8 kpc in the right panel). The identification of IRAS 17525−2506 is not certain (see Appendix).

3.3. Pattern speed of SiO maser sources

From the SiO radial-velocity data, we can calculate a pattern speed of the Galaxy without, in principle, the use of dynamical models (Tremaine, Weinberg 1984). However, because we are seeing the Galaxy in the edge-on direction, the method of computation must be modified from the original (Debattista et al. 2002). Furthermore, because the present sample is not evenly distributed in longitude with respect to the galactic center, we used a direct method, which is described as follows:

We only consider projected quantities onto the galactic plane. With the pattern speed, $\Omega_{\rm P}$, the surface density can be written as a function of time in galacto-centric coordinates as $\sigma(t,r,\phi) = \sigma(0,r,\phi-\Omega_{\rm P}\,t)$. The derivative with respect to time, $\partial\sigma/\partial t$, can be replaced by $-\Omega_{\rm P}\partial\sigma/\partial\phi$ in the continuity equation, leading to a pattern speed

$$\Omega_{\rm P} = \overline{div(\sigma\mathbf{v})} \,/\, \overline{\partial\sigma/\partial\phi}, \qquad (1)$$

where the bar indicates the surface integral over the disk area concerned. By Gauss's theorem, the surface integral can be changed to the integral along the curve enclosing the area. To make use of the present observed data, which are discrete quantities in density and velocity, they have to be made continuous. For this purpose, we approximate the discrete density/velocity profile by a sum of Gaussian-shape profiles as follows

$$\sigma(x,y) = \sum_i exp\{[(x-x_i)^2+(y-y_i)^2]/a^2\}/(\pi a^2), \qquad (2)$$

and the velocity fields by

$$\mathbf{v}(x,y) = \sum_i \mathbf{v}_i\, exp\{[(x-x_i)^2+(y-y_i)^2]/a^2\}/(\pi a^2), \qquad (3)$$

where the summation must be taken over all the sampled stars with known radial velocities. In this process, a smoothing parameter, a, is required to bridge vacant parts of the density profile in the concerned area (keeping

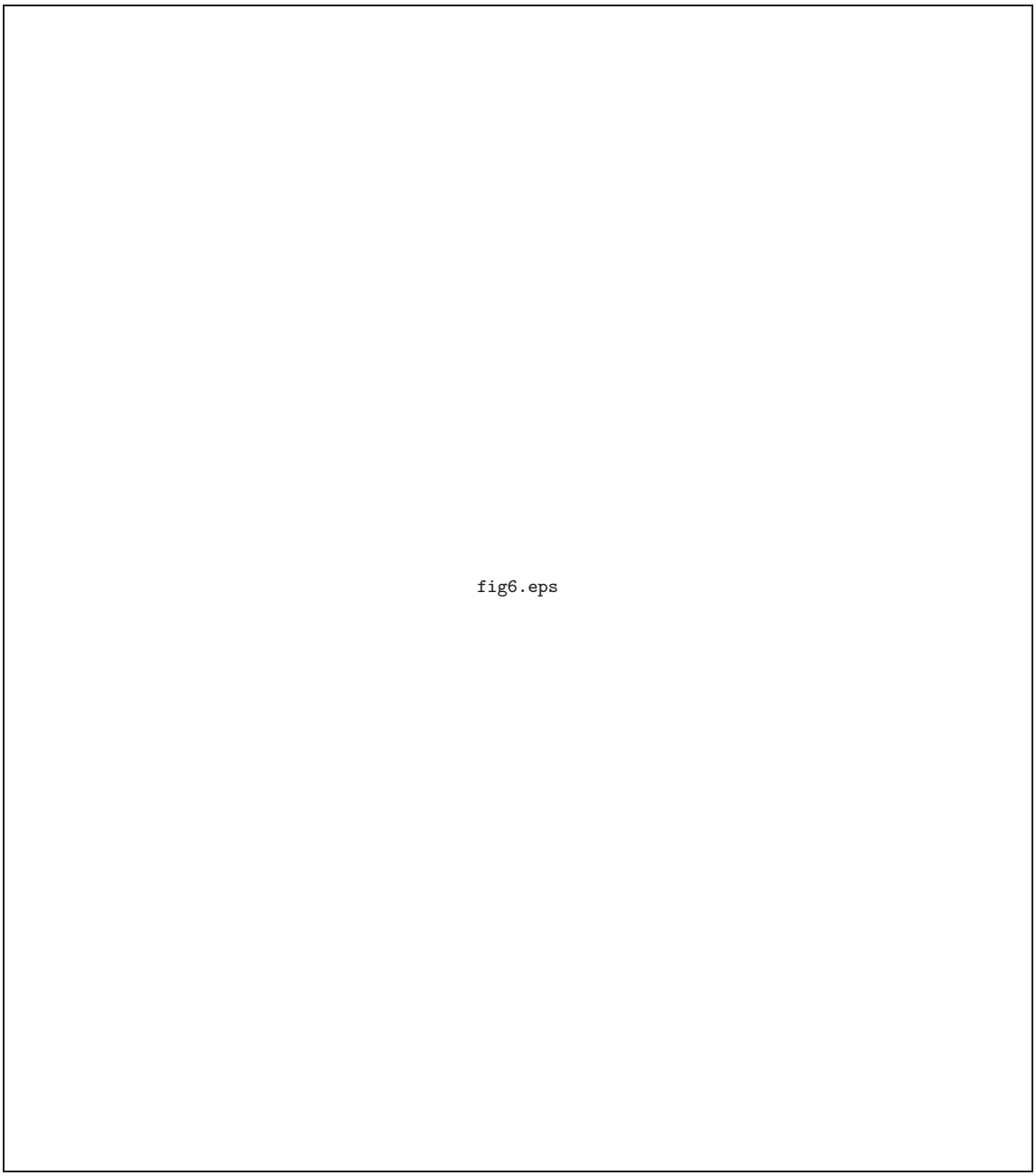

Fig. 6. Face-on view of the first quadrant of the Galaxy. The positions of the detected SiO sources are shown by open circles (from this paper) and squares (from the other papers quoted). The objects at $|b| > 10^{\circ}$ are indicated as circles with crosses. The sun is at the origin (shown as $\odot$) and the galactic center is at (8,0). A spiral model of the Galaxy (Taylor, Cordes 1993) is overlaid (thin curves for spiral and thin filled circles for HII regions).

as close as the true density as possible). We show later that the pattern speed that we obtain does not depend strongly on this parameter when 0.2 kpc $< a <$ 0.5 kpc.

In the first quadrant of the Galactic plane, we took four fan-shape areas between radii 1 and 2.5 kpc, 2.5 and 4 kpc, 4 and 5.5 kpc, and 5.5 and 7 kpc for integration, as illustrated in figure 7. The inflowing and outflowing mass fluxes at the boundary must be computed. For computing the inflow rate at $l = 0°$, we assume that all the particles at $l = 0°$ move with a tangential velocity of $v_t = 220$ km s^{-1} (because tangential velocities of the particles are unknown), which corresponds to the galactic rotation (with a flat rotation curve). This assumption is satisfied only in an approximate sense. Moreover, we assume that the mass inflow rates at the $l = 70°$ boundary are negligibly small. We used 547 (216 from this paper) SiO detected objects with color $-0.1 < C_{12} < 0.2$ in the strip $-10° < l < 70°$ and $|b| < 3°$. The luminosity distances were calculated by the same method for all the sources. Because the present sample involves objects with distances mostly below 7 kpc, we integrate only over the surface areas between 1 and 7 kpc.

Next, we calculated the inflow and outflow rates on the inner and outer arcs (for example, on arc BI and JA, in figure 7) of the fan-shape area ABIJ from the observed radial velocities (from equations 2 and 3). Adding the inflow rate from the $l = 0$ boundary (for example, the line AB), and dividing them by the average density differences at the boundaries (the denominator in equation 1), we obtain the pattern speeds in the four fan-shape areas between 1 and 7 kpc. The results are shown in figure 8. The lower panel shows the pattern speed in each fan-shape area between $D = 1$ and 7 kpc. The pattern speed obtained between 1 and 5.5 kpc for $a = 0.4$ kpc (the area, BEFI, adding the 3 separated fans into one) is

$$\Omega_{\rm P} = 21\ (\pm 13)\ {\rm km\ s^{-1}\ kpc^{-1}}, \quad (4)$$

where the value between the parentheses is the root mean square deviation from the average in the three areas. We calculated the pattern speed for $a = 0.05$ kpc to $a = 0.5$ kpc in 0.05 kpc steps. The computed pattern speed varies from 19 ($a = 0.25$ kpc) to 32 ($a = 0.05$ kpc) km s^{-1} kpc^{-1}. Here, we take a positive pattern speed to be prograde to the galactic rotation. The variation of the surface density, σ, at $l = 0°$ as a function of radius is shown in the upper panel of figure 8. When $a > 0.2$ kpc, the surface density seems adequately smoothed. When the smoothing parameter a is varied between 0.2 and 0.5 kpc, $\Omega_{\rm P}$ only changes between 19 and 24 km s^{-1} kpc^{-1}. Thus we consider that the value given in equation 4 is reasonable for the pattern speed of the SiO maser sources in the distance range $D = 1$–5.5 kpc in the present sample.

As shown in figure 7, the pattern speed tends to increase with decreasing radius from the Galactic center, though the number of SiO sources sampled at large distances (beyond 6 kpc) is insufficient. The pattern speed of the area, ABIJ (D =5.5–7 kpc), approaches 60 km s^{-1} kpc^{-1}, (45 kms^{-1} kpc^{-1} for $a = 0.25$ kpc, and 64 km s^{-1} kpc^{-1} for $a = 0.5$ kpc), This behavior of increasing pattern speed toward the Galactic center does not appear to be understandable in terms of a single pattern speed model for the Galaxy.

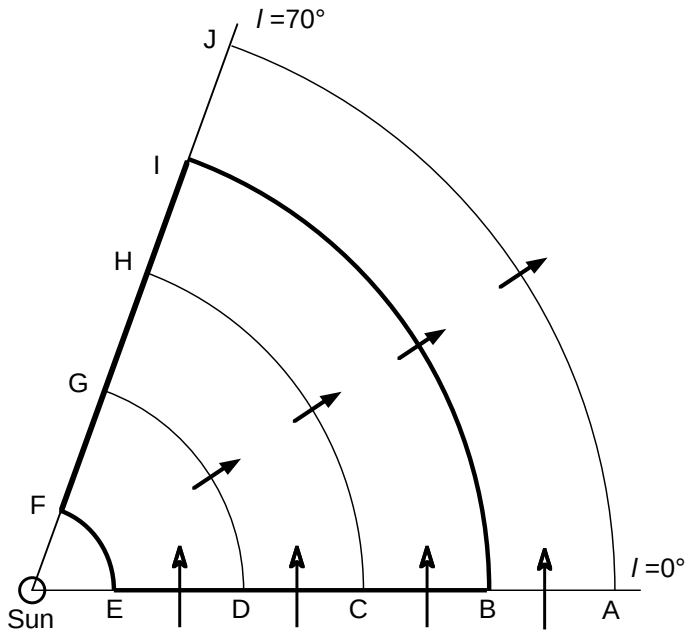

Fig. 7. Areas for integration. This figure indicate the first quadrant of the Galaxy, approximately the same area as in figure 6. The arrow indicates the flow of stars. The areas enclosed by ABIJ (D = 5.5–7 kpc), BCHI (D = 4–5.5 kpc), CDGH (D = 2.5–4 kpc), and DEFG (D = 1–2.5 kpc), are used for numerical integration. The area enclosed by BEFI shown in thick outline is used for taking the average.

Previously obtained values of the pattern speed of the Galaxy are widely different: for example, 19 km s^{-1} kpc^{-1} from gas-dynamical modeling of CO and HI near the galactic bar (Wada et al. 1994), 53 km s^{-1} kpc^{-1} from the analysis of Hipparcos late-type stellar data in the solar neighborhood (Dehnen 1999), 59 km s^{-1} kpc^{-1} from the OH/IR sources (Debattista et al. 2002), 20 km s^{-1} kpc^{-1} from dynamical modeling of the K-band spiral pattern (Martos et al. 2004). The value of the pattern speed obtained in the present paper, ~ 20 km s^{-1} kpc^{-1} gives the radius of co-rotation (to the galactic rotation) to be approximately 11 kpc, which is unreasonably large. However, a more recent hydrodynamic simulation with two pattern speeds (Bissantz et al. 2003) gives a good fit of the calculated gas pattern to the CO l–v diagram, resulting in $\sim$60 km s^{-1} kpc^{-1} and $\sim$20 km s^{-1} kpc^{-1} for the bar and spiral-arm pattern speeds, respectively. Thus, the tendency of the pattern speed to increase towards the Galactic center, which is found in this paper, can be interpreted as a manifestation of the two (inner fast and outer slow) pattern speeds for the Galactic bar and spiral arms. In this case, the corotation radius of the bar appears around 3.5 kpc and the radius of the inner Lindblad

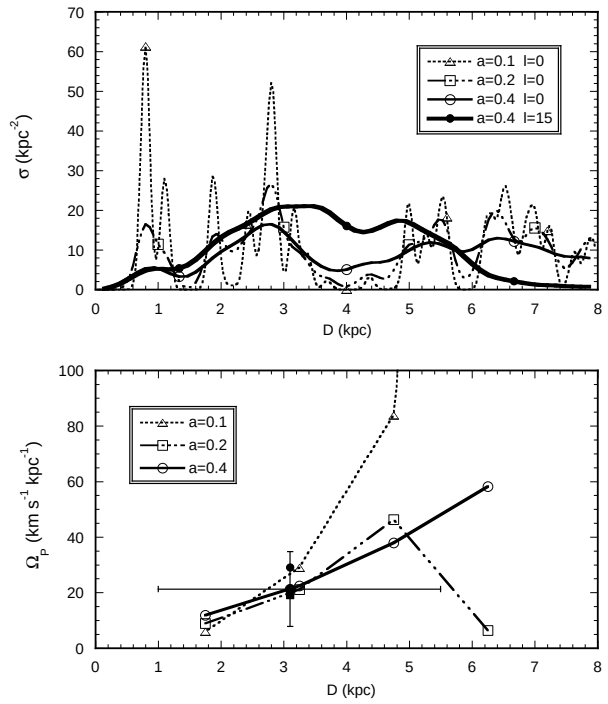

Fig. 8. Dependence of the results on the smoothing parameter, a. The upper panel shows the density profile along $l = 0°$, and the lower panel shows the pattern speed averaged over each 1.5 kpc in distance. The vertical error bar in the lower panel indicates the rms deviation of the three pattern speeds in the different areas, but the horizontal "error bar" indicates the inner and outer radii for the area used for the integration.

resonance of the two-armed spiral pattern around 3 kpc (Binney, Tremaine 1987; and see fig. 3 of Bissantz et al. 2003); this coincidence can possibly create the 3 kpc arm as described in Bissantz et al. (2003).

Though the pattern speed obtained in this paper does not depend on any dynamical models, the computation still involves several uncertain quantities such as the distances to the sources (we use luminosity distances), a mass inflow rate at $l = 0°$ given by a rotation curve ($v_0 = 220$ km s^{-1}), and a value of the smoothing parameter (we took $a = 0.4$ kpc as a representative value). Fortunately, mild variation of these parameters does not change the pattern speeds by large factors. Thus, we believe that the pattern speeds presented in this paper are close to the true ones.

4. Conclusion

We have surveyed 403 IRAS sources in the galactic disk and obtained 254 (239 new) detections in the SiO $J = 1$–0 $v = 1$ and 2 lines. The detections of SiO masers in IRAS sources with unknown characteristics constrain them to be O-rich evolved stars. The SiO l–v diagram in the area $-10° < l < 40°$ shows a lesser degree of concentration of SiO sources towards the molecular ring feature than does the OH 1612 MHz source l–v map, suggesting some difference of stellar type between SiO and OH objects.

We also identified all the SiO detected objects with 2MASS stars. We mapped the objects on the Galactic plane using luminosity distances based on the near- and mid-infrared flux densities. Combined with the radial-velocity data, we found the pattern speed of the SiO maser sources to be $\Omega_P = 21\ (\pm 13)$ km s^{-1} kpc^{-1} between galactocentric distances of 1 and 5.5 kpc, and $\Omega_P \sim 60$ km s^{-1} kpc^{-1} between distances 5.5 and 7 kpc.

We are grateful to graduate/undergraduate students, Mrs. Y. Eto, F. Ieda, M. Ioroi, R. Tamura, K. Watarai, and Ms. H. Fukushi for assistance with the observations during long runs. This research makes use of the SIMBAD database operated at CDS, Strasbourg, France, as well as data products from the Two Micron All Sky Survey, which is a joint project of the University of Massachusetts and the Infrared Processing and Analysis Center/California Institute of Technology, funded by the National Aeronautics and Space Administration and the National Science Foundation. This research was partly supported by Scientific Research Grant (C2) 12640243 of Japan Society for Promotion of Sciences.

Appendix. Individual Objects

We give SiO maser spectra for the detected objects in figures 9a–9p, and discuss individual objects here.

- 15060+0947 (=FV Boo) : This high-latitude star ($b = 53.27°$) exhibits an interesting double-peak emission profile in SiO lines in May 2003 (see top left in figure 5b) at $V_{\rm lsr} = -8.3$ and 2.1 km $^{-1}$; double peak SiO maser sources are relatively rare. Lewis (2002) listed this object as a dead OH/IR star, in which the OH 1612 MHz maser emission declined. The previous OH 1612 MHz line detection of this star (Eder et al. 1988) was at $V_{\rm lsr} = -16.3$ and 1.8 km s^{-1}, resulting in a stellar velocity of $V_{\rm lsr} = -7.1$ km s^{-1}. Engels, Lewis (1996) detected the triply peaked H_2O maser emission at $V_{\rm lsr} = -13.4$, -1.6, and 3.0 km s^{-1}, and Ita et al. (2001) detected SiO emission at slightly larger radial velocities in 2000 April, indicating a strong time variation. These facts suggest that this star is near the end of the AGB phase with varying mass loss rate.
- 16156−2837 (=V932 Sco) : This is a very bright star on the 2MASS K-band images ($K = 2.78$). The *General Catalog of Variable Stars* (Khopolov 1985) classified it as a variable star of Orion-type. The IRAS LRS class of this object is 27, implying that it has a silicate emission feature. A previous OH maser search was negative (te Lintel-Hekkert et al. 1991), but SiO masing was detected for the first time in this paper.
- 16342−3814 (=OH 344.07+5.84) and 18596+0315 (OH 37.12−.85): These are post-AGB stars with cool circumstellar envelopes ($C_{12} > 0.5$; Sahai et al. 1999). Though H_2O masers have been detected at

velocities outside the OH double peak velocity range (Zuckerman, Lo 1987 ; te Lintel-Hekkert et al. 1988; Gomez et al. 1994), SiO maser searches have been negative, which is consistent with the post-AGB star interpretation.

- 16473−2528 (=AF Sco) : This star was previously classified as a nova or cataclysmic variable, but has now been identified as a Mira-type variable (Duerbeck 1995). The IRAS LRS class is 29, indicating strong silicate features. Detections of the OH 1612 MHz and main lines (te Lintel-Hekkert et al. 1991; Lewis et al. 1995), and of SiO masers in the present paper, are all consistent with the Mira interpretation of this star.
- 17269−2625 (=V2311 Oph): The IRAS LRS spectral class for this object is 41 (indicating an 11 μm SiC feature), but Sylvester (1999) found the 10 μm silicate emission with UKIRT (=IRC−30300). Groenewegen et al. (1994) found the 18 μm silicate feature is noticeable in the IRAS LRS spectrum and gave the spectral type as $\geq$M8. The SiO detection in this paper secures that this is an O-rich AGB star. No OH masers have ever been detected.
- 17367−2319 (=V545 Oph): The OH 1612 MHz search was negative (te Lintel-Hekkert et al. 1991). This is a strong IRAS source ($F_{12} = 55.8$ Jy) with LRS class 26 (silicate feature). Groenewegen et al. (1999) detected CO $J = 2$–1 emission from this star at $V_{\rm LSR} = -18.7$ km s^{-1}, which coincides with the SiO velocity at $V_{\rm lsr} = -19.2$ km s^{-1} in the present paper.
- 17525−2506 (=OH 4.417 +.044) : This object occupies a unique position in the two-color diagram (figure 2), because the IRAS Point Source Catalog gives a very high 60 μm flux for it (F_{60}=1007 Jy, but F_{12}=11.3 Jy). However, this is due to contamination by a surrounding young stellar object (IRAS 17522−2504 with F_{60}=1007 Jy), in a star forming region. The positions of the OH 1612 MHz maser (Becker et al. 1992; Sevenster et al. 1997) coincide with those of MSX5CG004.4181+00.0438 within 4″. A close look at 2MASS images toward this object and at the DENIS database give several faint red stars around the OH positions, which are equally dubious as candidates. SiO masing from this object is relatively strong (see figure 9d).
- 17559−2848 (=V4336 Sgr) : This is a relatively strong IRAS source ($F_{12} = 29.3$ Jy) with LRS class 25 (silicate emission). This is located in the Sgr I optical window and Glass et al. (1995) measured the period of NIR light variation of 557 d. OH 1612 MHz double peaks were detected (te Lintel-Hekkert et al. 1991; Sevenster et al. 1997) resulting in a stellar velocity $V_{\rm lsr} = -39.1$ km s^{-1}, which is consistent with SiO detection at $V_{\rm lsr} = -40.0$ km s^{-1} (present paper).
- 17599−2603: This object (MSX5C_G004.4403-01.8761) is located close to the globular cluster, Terzan 10 ($\sim 1.4'$). Considering the distance of this glubular cluster (5.7 kpc; Harris 1996), we cannot deny a possibility of this relatively strong middle-IR source ($F_{12} = 8.6$ Jy) to be a member of this glubular cluster. Because the radial velocity of this glubular cluster has not been measured unfortunately, the SiO radial velocity ($V_{\rm lrs} = 81.7$ km s^{-1}) cannot be used to judge the membership.
- 18038−1614 : The IRAS LRS class of this source is 14, indicating a featureless spectrum. However, we can see silicate emission features at 9.8 and 18 micron in the raw LRS spectrum (Olnon et al. 1986). The SIMBAD database indicates that this is a carbon star, but the detection of SiO masers (present paper) excludes such a possibility. Searches for the CO $J = 2$–1 and 1–0 lines and OH 1612 MHz emission were negative (Groenewegen et al. 2002; te Lintel-Hekkert et al. 1991; Le Squeren et al. 1992).
- 18210−1359 : The 2MASS images give two equally red candidate stars: one 16″ east and the other 20″ west of the IRAS position. The MSX map also gives two point-like objects at similar positions. We observed and detected SiO masers in the MSX point source 16″ east, MSX5CG017.3984−00.3836, which the brighter of the two in K magnitude (K =6.53 and $H - K$ =2.06). The SIMBAD assignment of this object (IRAS 18210−1359) to GAL 017.4−00.4 (supernova remnant candidate) is inappropriate.
- 18213−1739 : 2MASS images show a very red star [$R.A. = 18^{\rm h}24^{\rm m}15.12^{\rm s}$, $Dec = -17°37'44.3''$, J2000, with K =11.20 and $H - K$ =3.75] within 3″ the IRAS position, while the DENIS database gives 2 brighter stars with $K = 8.70$ and 8.72 at almost the same position. The difference in the K magnitudes between 2MASS and DENNIS can be attributed to a time variation. The SIMBAD assignment of this IRAS source as an A2 star, HD 169195 (more than 1' away from the IRAS position), seems inappropriate. SiO masers were detected for the first time in this paper and the previous OH search (te Lintel-Hekkert et al. 1991) was negative.
- 18417−0205 : Felli et al. (2002) classified this object (ISOGAL−PJ184418.5−020153) as a YSO candidate with confidence level 0. SiO masers were detected during this program. The DENIS K magnitude of the identified star is 8.68, and the 2MASS database gives $K = 7.84$ with $H - K = 1.89$, suggesting that it is a variable star. These facts are enough to conclude that this is an evolved object.
- 18588+0428 (=OH 38.101−0.125) : This source has been classified as a post-AGB star in the SIMBAD database. However, the detection of relatively strong SiO masers at $V_{\rm lsr} = 52$ km s^{-1}, which is consistent with the center velocity of the OH maser double peaks (Lewis 1994; Sevenster 2002), excludes the possibility of a post-AGB star. The IRAS LRS class is 39, indicating a silicate absorption feature at 9.8 μm. The 2MASS database gives a very red star ($K = 8.57$ and $H - K = 3.29$) near the IRAS position.

- 19093−3256 (=V342 Sgr) : This is a bright Mira ($P = 372$ d) with $F_{12} = 318$ Jy and $K = 1.3$ located out of the Galactic plane at $[(l,b) = (4.79°, -18.44°)]$. The SiO $J = 2$–1 $v = 1$ (Haikala et al. 1994) and $J = 1$–0 $v = 1$ and 2 masers (present paper) have been detected at $V_{\rm lsr} = 40.8$ km s^{-1}, which is consistent with the CO $J = 1$–0 radial velocity at $V_c = 37.7$ km s^{-1} (Nyman et al. 1992). The OH maser search was negative (te Lintel-Hekkert et al. 1991).

References

Alcolea, J., Bujarrabal, V., & Gomez-Gonzalez, J. 1990, A&A, 231, 431

Becker, R. H., White, R. L., & Proctor, D. D. 1992, AJ, 103, 544

Benson, P. J., & Little-Marenin, I. R. 1996, ApJS, 106, 579

Binney, J., Gerhard, O. E., Stark, A. A., Bally, J., & Uchida, K. I. 1991, MNRAS, 252, 210

Binney, J., & Tremaine, S. 1987, Galactic Dynamics (Princeton Univ. Press, Princeton), 194

Bissantz, N., Englmaier, P. & Gerhard, O. 2003, MNRAS, 340, 949

Blommaert, J. A. D. L., van Langevelde, H. J., & Michiels, W. F. P. 1994, A&A, 287, 479

Caswell, J. L., 1999, MN, 308, 683

Chengalur J.N., Lewis, B.M., Eder J., & Terzian Y. 1993, ApJS, 89, 189

Dame, T. M., Hartmann, D., & Thaddeus, P. 2001, ApJ, 547, 792

Debattista, V. P., Gerhard, O., & Sevenster, M. N. 2002, MNRAS, 334, 355

Deguchi, S., Matsumoto, S., & Wood, P. R. 1998, PASJ, 50, 597

Deguchi, S., Fujii, T., Izumiura, H., Kameya, O., Nakada, Y., Nakashima, J., Otsubo, T., & Ukita, N. 2000a, ApJS, 128, 571

Deguchi, S., Fujii, T., Izumiura, H., Kameya, O., S. Nakada, Y., & Nakashima, J. 2000b, ApJS, 130, 351

Deguchi, S., Fujii, T., Matsumoto, S. Nakashima, J., & Wood, P. 2001, PASJ, 53, 293

Deguchi, S., Fujii, T., Nakashima, J., Wood, P. R. 2002, PASJ, 54, 719

Deguchi, S., Imai, H., Fujii, T., Glass, I. S., Ita, Y., Izumiura, H., Kameya, O., Miyazaki, A., Nakada, Y., & Nakashima, J., 2004, PASJ, 56, 261

Deguchi, S., Nakashima, J., & Balasubramanyam, R. 2004, PASJ, 53, 305

Dehnen, W., 1999, ApJ, 524, L35

Dwek, E., Arendt, R. G., Hauser, M. G., Kelsall, T., Lisse, C. M., Moseley, S. H., Silverberg, R. F., Sodroski, T. J., & Weiland, J. L. 1995, ApJ, 445, 716

Duerbeck, H. W. 1995, IBVS 4219, 1

Eder, J., Lewis, B. M., & Terzian, Y. 1988, ApJS, 66, 183

Egan M. P., Price S. D., Moshir M., Cohen M., Tedesco E. F., Murdock T. L., Zweil A., Burdick S., Bonito N., Gugliotti G.M., Duszlak J. 1999, Air Force Research Laboratory Technical Report No. AFRL-VS-TR-1999-1522 (availabe at IPAC, ⟨http://irsa.ipac.caltech.edu/applications/MSX/⟩ with the MSX catalog)

Engels D., & Heske A. 1989, A&AS, 81, 323

Engels, D., & Lewis, B. M. 1996, A&AS, 116, 117

Feast, M. W. 1996, MNRAS, 278, 11

Feast, M. W. & Whitelock, P. A. 2000, MNRAS.317, 460

Felli, M., Testi, L., Schuller, F., & Omont, A. 2002, A&A, 392, 971

Fux, R. 1999, A&A, 345, 787

Galt, J. A., Kwok, S., & Frankow, J. 1989, AJ, 98, 2182

Glass, I. S., Whitelock, P. A., Catchpole, R. M., & Feast, M. W. 1995, MNRAS 273, 383

Gomez, Y. Moran, J. M., & Rodriguez, L. F. 1990, RMxAA, 20, 55

Gomez, Y., Rodriguez, L. F., Contreras, M. E., & Moran, J. M. 1994, RMxAA, 28, 97

Groenewegen, M. A. T. 1994, A&A, 290, 207

Groenewegen, M. A. T., Baas, F. Blommaert, J. A. D. L. Stehle, R. Josselin, E. Tilanus, R. P. J. 1999, A&AS, 140, 197

Groenewegen, M. A. T., Sevenster, M., Spoon, H. W. W., & Perez, I. 2002, A&A, 390, 501

Haikala, L. K., Nyman, L.-Å., & Forsström, V., 1994, A&AS, 103, 107

Harris, W. E. 1996, AJ, 112, 1487

Imai, H., Deguchi, S., Fujii, T., Glass, I. S., Ita, Y., Izumiura, H., Kameya, O., Miyazaki, A., Nakada, Y., & Nakashima, J., 2002, PASJ, 54, L19

Ita, Y., Deguchi, S., Fujii, T., Kameya, O., Miyoshi, M., Nakada, Y., Nakashima, J., & Parthasarathy, M. 2001, A&A, 376, 112

Izumiura, H., Deguchi, S., Fujii, T., Kameya, O., Matsumoto, S., Nakada, Y., Ootsubo, T., & Ukita N. 1999, ApJS, 125, 257

Jewell, P.R., Snyder, L.E., Walmsley, C.M., Wilson, T.L., & Gensheimer, P.D., 1991, A&A, 242, 211

Jiang, B. W., Deguchi, S., Yamamura, I., Nakada, Y., Cho, S. H., & Yamagata, T. 1996, ApJS, 106, 463

Jiang, B.W., Deguchi,S., & Ramesh, B. 1999, PASJ, 51. 95

Khopolov 1985, IBVS, 2681, 1

Kwok, S., Volk, K., & Bidelman, W. P. 1997, ApJS, 112, 557

Le Squeren, A. M., Sivagnanam, P., Dennefeld, M., & David, P. 1992, A&A, 254, 133

Lewis, B.M. 1994, ApJS, 93, 549

Lewis, B. M. David, P. & Le Squeren, A. M. 1995, A&AS, 111, 237

Lewins, B. M., & Engels, D. 1995, MNRAS, 274, 439

Lewis, B. M. 2000, ApJ, 533, 959

Lewis, B. M. 2002, ApJ, 576, 445

Martos, M., Hernandez, X., Yanez, M., Moreno, E., Pichardo, B. 2004, MNRAS, 350, L47

Messineo M., Habing H.J., Sjouwerman L.O., Omont A., & Menten K.M. 2002, A&A393, 115

Nakashima, J., Jiang, B.W., Deguchi, S., Sadakane, K., & Nakada, Y. 2000, PASJ, 52, 275

Nakashima, J., & Deguchi, S. 2003a, PASJ, 55, 203

Nikolaev S., Weinberg M. D. 1997, ApJ487, 885

Nyman, L.-A. Booth, R. S. Carlstrom, U. Habing, H. J. Heske, A. Sahai, R. Stark, R. van der Veen, W. E. J. C. & Winnberg, A.1992, A&AS, 93, 121

Nyman, L.-Å., Hall, P.J., & Olofsson, H. 1998, A&AS, 127, 185

Olnon, F. M., Raimond, E. R., & IRAS Science team, 1986, A&AS, 65, 607

Sahai, R., te Lintel-Hekkert, P., Morris, M., Zijlstra, A., & Likkel, L., 1999, ApJ, 514, L115

Sevenster, M.N. 2002, AJ, 123, 2788

Sevenster, M. N., Chapman, J. M., Habing, H., Killeen, N. E. B., & Lindqvist, M. 1997, A&AS, 122, 79

Sevenster, M. N., van Langevelde, H. J., Moody, R. A., Chapman, J. M., Habing, H. J., Killeen, N. E. B. , 2001, A&A, 366, 481
Sivagnanam, P., Le Squeren, A. M., Minh, F. Tran, & Braz, M. A. P. 1990, A&A233, 112
Sylvester, R. J. 1999, MNRAS, 309, 180
Taylor, J. H., & Cordes, J. M. 1993, ApJ, 411, 674
te Lintel-Hekkert, P., Habing, H. J., Caswell, J. L., Norris, R. P., & Haynes, R. F., 1988, A&A, 202, L19
te Lintel Hekkert, P., Versteege-Hensel, H. A., Habing, H. J., & Wiertz, M., 1989, A&AS, 78, 399
te Lintel-Hekkert, P., Caswell, J. L., Habing, H. J., Haynes, R. F., & Norris, R. P. 1991, A&AS, 90, 327
Tremaine, S. T., & Weinberg, M. D. 1984, ApJ, 282, L5
Unavane, M., Gilmore G., Epchtein N., Simon G., Tiphéne D., & de Batz B. 1998, MNRAS, 295, 119
van der Veen, W.E.C.J., & Habing, H.J. 1988, A&A, 194, 125
Wada, K., Taniguchi, Y., Habe, A., Hasegawa, T. 1994, ApJ, 437, L123
Zuckerman, B., & Lo, K. Y., 1987, A&A, 173, 263

Table 1. List of detections

IRAS name	SiO $v=1$, $J=1$–0				SiO $v=2$, $J=1$–0				Obs.Date	V_{ave}	Prev.	Obs.
	V_{peak}	T_{peak}	$Flux$	RMS	V_{peak}	T_{peak}	$Flux$	RMS			SiO	OH
	(km s^{-1})	(K)	(K km s^{-1})	(K)	(km s^{-1})	(K)	(K km s^{-1})	(K)	(yymmdd.d)	(km s^{-1})		
14251−3246	−22.4	0.304	1.021	0.056	−19.3	0.226	0.538	0.061	010410.0	−20.9		y[4]
14402−3645	51.6	0.236	0.285	0.066	50.1	0.401	0.943	0.079	010410.0	50.9		
15060+0947	−8.2	1.047	5.514	0.052	−8.3	1.191	4.505	0.071	030512.0	−8.3	y[10]	y[11]
15576−1212	−3.4	8.152	26.274	0.191	−3.4	4.927	23.875	0.223	030521.0	−3.4		y[4]
16038−2230	45.0	0.924	4.262	0.098	41.6	1.063	4.533	0.117	030528.0	43.3		n[4]
16063−3227	−44.0	1.030	5.543	0.115	−39.8	1.053	3.479	0.141	030524.0	−41.9		n[4,12]
16091−1655	47.5	1.450	3.701	0.109	47.1	1.183	2.312	0.144	030523.0	47.3		y[4]
16156−2837	−8.4	2.900	5.637	0.129	−8.3	2.062	6.519	0.175	030523.0	−8.4		n[4]
16309−1949	7.0	0.617	1.853	0.068	6.8	0.482	1.395	0.087	030529.0	6.9		
16322−2205	−24.9	1.999	8.356	0.112	−24.9	3.095	11.301	0.155	030523.0	−24.9		n[4]
16339−2712	31.6	0.257	0.334	0.058	32.2	0.311	0.723	0.070	030524.0	31.9		
16388−2939	14.9	4.981	10.377	0.115	15.0	6.727	14.519	0.136	030525.0	14.9		
16473−2528	58.3	6.521	15.708	0.103	58.2	3.401	8.413	0.134	030522.0	58.3		y[4]
16482−2039	−5.9	1.269	4.369	0.079	−4.6	1.177	2.901	0.117	030527.0	−5.3		n[4]
16559−2557	−10.1	4.087	13.368	0.107	−10.1	3.069	10.039	0.133	030522.0	−10.1		n[4]
17100−3521	−51.8	1.021	3.019	0.086	52.4	0.659	2.065	0.082	020221.2	−52.1		y[4]
17103−0559	−17.4	6.564	16.531	0.138	17.2	5.001	15.546	0.171	030521.0	−17.3		y[4]
17115−3538	−64.8	0.240	0.590	0.041	−64.5	0.308	0.694	0.065	021214.4	−64.7		
17122−2019	4.0	1.654	6.084	0.116	4.8	1.585	5.382	0.143	030528.0	4.4		n[4]
17181−1901	−18.2	0.463	1.397	0.063	−18.3	0.392	0.949	0.081	030529.0	−18.2		
17186−3445	66.4	1.603	5.570	0.048	67.2	1.301	3.419	0.048	021214.4	66.8		
17197−3517	59.8	0.473	0.742	0.067	59.5	0.629	1.547	0.068	020307.3	59.7		y[13]
17205−1609	7.3	0.273	1.296	0.064	0.9	0.318	1.249	0.088	030530.0	4.1		n[4]
17220−3118	58.4	0.271	0.504	0.056	58.2	0.220	1.021	0.056	020604.1	58.3		
17232−3620	−46.7	0.321	0.882	0.040	47.2	0.273	0.527	0.038	020307.3	−46.9		
17255−2928	−81.4	0.148	0.145	0.045	76.6	0.226	0.425	0.055	020604.1	−76.6		
17264−3521	−22.7	0.585	1.657	0.075	21.9	0.758	3.882	0.094	020307.3	−22.3	n[9]	y[13]
17269−2625	−25.2	0.297	0.428	0.079	27.3	0.475	0.878	0.118	030514.0	−26.3		
17318−2342	−8.5	0.641	1.527	0.087	−7.9	0.529	1.785	0.106	030516.0	−8.2		
17323−0556	42.2	0.314	1.608	0.073	43.1	0.477	1.556	0.092	030521.0	42.7		
17352−3252	33.4	0.268	0.841	0.060	29.0	0.348	1.294	0.059	020602.0	31.2		
17360−3012	3.3	1.771	9.242	0.117	2.4	5.483	19.820	0.117	020601.9	2.9		y[13]
17361−2807	−22.4	0.325	0.556	0.082	−22.1	0.474	1.273	0.076	010526.0	−22.2		y[13]
17367−2319	−19.5	4.411	11.613	0.162	−18.9	5.580	14.748	0.214	030516.0	−19.2		n[4]
17371−2718	−121.6	0.315	0.360	0.082	−120.7	0.406	0.830	0.103	020604.1	−121.2		n[4]
17383−3144	23.0	2.626	7.240	0.186	20.2	1.558	5.787	0.181	020523.1	21.6		y[13]
17388−2450	−107.1	0.302	1.312	0.055	−108.0	0.356	0.884	0.055	020224.2	−107.6		n[4]
17390−3014	−23.7	0.501	1.181	0.059	23.6	0.483	1.203	0.062	010311.3	−23.7		y[13]
17393−3004	−6.7	6.338	51.478	0.117	−7.2	7.136	60.222	0.117	020602.0	−6.9		y[13]
17398−3016	—	—	—	0.060	17.2	0.269	0.818	0.067	010311.3	−17.2		
17403−0658	30.6	1.049	5.973	0.112	33.3	0.871	3.273	0.139	030521.0	32.0		
17406−2614	157.9	0.292	0.589	0.063	154.4	—	—	—	030514.2	157.9		
17412−2706	−32.1	0.863	2.335	0.069	32.2	0.853	2.400	0.068	010404.1	−32.2		
17413−2508	−59.6	0.477	0.920	0.060	60.5	0.336	0.843	0.061	020527.1	−60.0		y[4]
17414−2531	146.4	0.708	0.294	0.054	147.9	2.323	0.344	0.074	020527.1	147.1		
17423−0511	−30.6	0.530	1.225	0.071	−29.9	0.594	1.029	0.097	030523.1	−30.2		
17424−2622	−93.2	0.635	2.035	0.083	90.4	0.440	1.627	0.081	020529.0	−91.8		
17426−2535	206.7	0.262	0.440	0.068	208.3	0.299	0.985	0.093	020527.1	207.5		
17434−2354	4.0	0.247	0.737	0.060	2.7	0.287	0.683	0.060	020519.0	3.4		
17443−2519	31.2	0.443	0.415	0.070	30.9	0.514	1.719	0.070	010308.3	31.1	n[6]	y[4,13]
17451−2731	9.7	0.244	1.222	0.046	8.9	0.279	0.719	0.047	010308.3	9.3		
17459−3057	32.0	4.402	16.521	0.152	29.5	3.777	17.369	0.151	020602.0	30.8		y[13]
17465−0731	22.1	0.936	2.788	0.068	21.9	0.745	2.169	0.090	030527.1	22.0		
17468−2932	52.9	0.528	2.308	0.076	52.9	0.586	1.991	0.080	010525.0	52.9		
17471−0525	−16.8	0.311	0.290	0.073	−17.1	0.591	0.707	0.109	030523.1	−16.9		
17473−2549	−62.8	0.636	1.508	0.086	61.1	0.729	2.428	0.086	020311.3	−62.0		y[13]
17487−2537	−9.7	0.369	1.443	0.042	−9.7	0.537	2.203	0.041	010310.2	−9.7		
17488−2450	−120.4	0.196	0.512	0.043	118.8	0.199	0.425	0.051	010403.3	−119.6		

Table 1. (Continued)

IRAS name	SiO $v=1$, $J=1$–0				SiO $v=2$, $J=1$–0				Obs.Date	V_{ave}	Prev.	Obs.
	V_{peak}	T_{peak}	*Flux*	*RMS*	V_{peak}	T_{peak}	*Flux*	*RMS*			SiO	OH
	(km s^{-1})	(K)	(K km s^{-1})	(K)	(km s^{-1})	(K)	(K km s^{-1})	(K)	(yymmdd.d)	(km s^{-1})		
17488−2532	50.3	1.206	5.785	0.044	48.5	0.959	3.741	0.043	010310.2	49.4		y[13]
17489−2207	−4.9	0.494	2.373	0.099	−9.2	0.507	2.049	0.094	020531.0	−7.1		
17490−2711	−84.9	0.722	2.087	0.077	−84.6	1.173	3.222	0.081	020307.3	−84.7		
17493−2139	38.1	0.143	0.489	0.046	37.5	0.253	0.507	0.049	010308.3	37.8		
17504−2149	103.0	0.330	0.920	0.096	103.5	0.264	0.015	0.093	020527.1	103.2		
17505−3143	2.1	0.372	0.101	0.091	1.3	0.386	1.224	0.097	020604.0	1.7	y[6]	y[4]
17515−2747	−123.2	0.435	0.455	0.090	−122.6	0.463	1.045	0.102	030512.1	−122.9		
17525−2506	−1.0	2.578	4.244	0.079	−1.4	2.244	4.811	0.084	020604.0	−1.2		y[13]
17535−2421	221.6	0.162	0.386	0.058	221.1	0.178	0.004	0.077	020602.1	221.4		
17536−1950	−5.9	0.962	2.195	0.120	−5.7	1.151	3.611	0.145	030527.3	−5.8		
17538−2329	16.0	0.361	1.612	0.068	15.8	0.435	2.148	0.065	010525.0	15.9		
17540−2856	−146.4	0.711	1.486	0.098	−147.2	0.550	1.385	0.110	030514.2	−146.8		
17548−2652	186.2	0.615	1.533	0.096	186.8	0.557	1.396	0.097	030511.1	186.5		
17559−2848	−40.1	1.383	6.506	0.128	−37.4	1.361	6.027	0.126	020522.2	−38.7		y[13]
17573−2259	65.7	0.896	0.820	0.162	65.5	0.962	1.323	0.160	010527.0	65.6		
17575−2644	−0.1	0.183	0.899	0.051	−0.1	0.389	1.046	0.051	020307.4	−0.1		n[4]
17581−1910	22.5	0.236	0.851	0.052	22.7	0.275	0.184	0.055	020312.4	22.6		n[4]
17586−2152	11.3	0.618	1.964	0.071	10.8	0.704	1.306	0.072	020223.2	11.0		
17591−1829	66.5	0.615	2.325	0.070	65.2	0.574	1.947	0.081	020314.3	65.9		
17594−2201	18.5	0.693	2.241	0.041	17.3	0.676	2.939	0.043	010310.2	17.9		
17596−1944	17.5	0.440	1.829	0.084	11.7	0.403	1.698	0.079	020521.1	14.6		n[4]
17599−2603	81.7	0.180	0.699	0.051	81.7	0.229	0.791	0.051	020316.3	81.7		
18002−2154	92.7	0.244	0.580	0.048	92.3	0.282	0.822	0.052	010310.2	92.5		
18007−1833	−17.3	2.878	6.277	0.133	−17.6	2.354	4.846	0.138	020523.1	−17.4		
18008−2701	209.4	0.147	0.508	0.031	209.7	0.127	0.561	0.039	010310.3	209.6		
18009−1830	119.3	0.191	0.679	0.047	117.4	0.202	0.783	0.058	020426.0	118.4		
18013−2700	−87.0	0.283	0.618	0.042	−86.7	0.305	0.585	0.041	010310.3	−86.8		
18020−1820	42.7	0.286	0.248	0.061	42.4	0.432	1.426	0.064	020426.1	42.5		y[4]
18021−1653	77.5	0.425	0.746	0.067	77.5	0.827	1.460	0.069	020219.3	77.5		
18022−2656	−79.2	0.240	0.324	0.073	−80.0	0.341	0.521	0.081	020311.3	−79.6		
18025−2354	−3.8	0.804	1.516	0.111	−3.4	0.948	1.330	0.114	020523.0	−3.6		y[13]
18029−2048	18.8	1.035	1.749	0.138	18.3	0.815	1.343	0.131	010522.0	18.6		
18032−1859	−38.6	0.215	0.427	0.061	−38.2	0.535	1.289	0.082	030528.3	−38.4		
18034−2441	6.6	1.830	4.183	0.035	6.5	1.392	4.796	0.034	010310.3	6.5		y[4]
18035−2529	3.6	2.622	4.718	0.166	4.0	2.324	5.337	0.167	020223.2	3.8		y[4]
18036−2049	47.0	0.567	0.931	0.079	47.0	0.549	1.528	0.088	020602.1	47.0		n[4]
18038−1614	−15.4	0.596	1.929	0.072	−15.4	0.479	2.230	0.072	010525.1	−15.4		n[4,7]
18041−2242	41.7	0.163	0.274	0.051	42.2	0.376	0.556	0.054	020305.4	41.9		
18048−2309	69.6	2.480	13.306	0.089	69.1	1.538	8.660	0.095	020522.2	69.3		
18051−1638	104.8	0.498	1.594	0.076	104.9	0.407	1.052	0.097	030512.1	104.8		
18081−1451	−25.2	0.326	0.824	0.048	24.0	0.175	0.525	0.046	020531.0	−24.6		
18096−1645	55.0	0.148	0.631	0.051	49.0	0.258	0.919	0.060	030512.1	52.0		
18099−1449	1.7	0.244	0.566	0.064	−0.5	0.380	0.879	0.058	010520.0	0.6		
18100−1250	80.2	0.237	0.591	0.035	79.5	0.188	0.412	0.037	020222.3	79.8		
18108−1654	—	—	—	0.064	30.6	0.544	0.394	0.066	020531.0	30.6		
18114−1934	50.9	0.685	2.140	0.085	51.1	0.494	2.138	0.086	020523.1	51.0		
18115−2139	5.2	1.421	4.957	0.087	3.7	0.701	2.632	0.092	020219.3	4.5		y[4.13]
18118−1615	185.6	0.150	0.521	0.038	184.7	0.183	0.271	0.049	020604.0	185.2		
18119−2035	82.6	0.387	1.524	0.056	82.9	0.470	0.214	0.080	030511.0	82.8		
18128−2158	70.1	0.445	2.163	0.084	70.4	0.362	1.497	0.088	020523.1	70.3		n[12]
18129−1620	13.7	0.774	1.935	0.068	13.7	0.572	1.370	0.098	030511.1	13.7		y[14]
18135−1505	68.6	0.184	0.295	0.046	69.1	0.213	0.637	0.046	020219.4	68.8		
18137−1549	58.1	0.396	2.010	0.055	58.4	0.350	1.899	0.055	020519.2	58.3		
18139−1937	46.6	0.274	0.717	0.050	51.4	0.121	0.179	0.049	020523.1	49.0		
18143−2128	209.1	0.377	0.636	0.088	209.1	0.805	1.443	0.116	030511.1	209.1		n[4]
18145−1604	−16.0	0.305	1.309	0.076	15.6	0.336	1.797	0.093	030512.1	−15.8	y[14]	
18146−1709	4.7	1.168	5.652	0.100	3.2	1.033	6.330	0.104	020426.2	3.9		
18147−0946	27.1	0.197	0.357	0.029	27.4	0.160	0.392	0.033	020222.3	27.2		y[4]

Table 1. (Continued)

	SiO $v=1$, $J=1$–0				SiO $v=2$, $J=1$–0						Prev.	Obs.
IRAS name	V_{peak} (km s^{-1})	T_{peak} (K)	$Flux$ (K km s^{-1})	RMS (K)	V_{peak} (km s^{-1})	T_{peak} (K)	$Flux$ (K km s^{-1})	RMS (K)	Obs.Date (yymmdd.d)	V_{ave} (km s^{-1})	SiO	OH
18154−1727	27.0	1.518	3.188	0.128	26.4	1.372	2.821	0.130	020523.1	26.7		
18156−2121	6.3	0.681	1.881	0.086	6.4	0.735	3.881	0.088	020531.1	6.4		n[4]
18173−1100	133.0	0.477	1.292	0.086	133.6	0.684	1.974	0.099	030514.2	133.3		
18189−1648	130.9	0.880	2.900	0.164	131.5	1.139	2.806	0.194	010524.1	131.2		
18196−1608	40.2	0.455	3.173	0.083	42.4	0.586	2.339	0.096	020604.0	41.3		
18198−1342	68.0	0.740	1.647	0.098	70.1	0.528	1.722	0.084	010403.1	69.1		y[15]
18199−1144	75.4	0.775	1.344	0.161	75.9	0.947	1.748	0.168	010524.1	75.7		
18207−1029	38.9	1.784	5.246	0.160	39.1	1.371	5.028	0.157	010524.0	39.0		y[4]
18207−1221	30.2	0.486	1.217	0.142	26.8	0.445	2.658	0.137	010524.1	28.5		
18210−1359	−44.0	0.642	2.020	0.080	−44.1	0.664	1.943	0.099	030512.2	−44.0		
18213−1739	165.7	0.179	0.155	0.051	166.0	0.365	0.296	0.063	020531.1	165.8		n[4]
18216−1552	—	—	—	0.068	−4.4	0.684	0.639	0.078	020519.2	−4.4		y[7]
18222−1029	126.3	1.894	8.700	0.128	126.4	1.441	6.442	0.163	010525.0	126.3		
18224−0932	73.0	0.339	1.198	0.069	70.6	0.346	1.105	0.073	020521.2	71.8		
18227−1205	−20.2	0.335	0.929	0.071	−20.8	0.489	1.398	0.093	030512.2	−20.5		
18231−1500	−33.3	0.320	0.923	0.087	−38.2	0.584	2.318	0.089	020531.1	−35.8		
18232−1003	80.4	0.333	0.849	0.054	79.8	0.324	0.988	0.058	020222.3	80.1		
18235−1038	97.9	0.502	1.579	0.061	97.5	0.465	1.329	0.067	020222.3	97.7		n[4]
18236−1422	78.7	0.744	2.232	0.099	75.4	0.515	2.577	0.102	020523.1	77.0		
18241−1115	−0.4	0.988	1.831	0.119	−0.2	0.677	1.584	0.113	010524.0	−0.3		
18245−0552	−2.5	0.304	0.529	0.049	1.1	0.362	1.266	0.051	010524.1	−0.7		y[7]
18254−1106	−46.4	2.523	7.022	0.094	−46.6	2.849	7.738	0.109	020313.3	−46.5		
18254−1118	26.8	0.855	2.058	0.064	26.8	0.967	3.259	0.078	020218.4	26.8	y[16]	y[17]
18260−1142	−4.7	0.582	2.299	0.076	−4.2	0.460	2.564	0.096	030512.1	−4.4		
18266−1411	−10.3	0.463	1.382	0.065	−9.9	0.631	1.974	0.075	020218.4	−10.1		
18268−0417	59.2	0.269	0.957	0.728	60.0	0.505	1.761	0.096	030516.3	59.6		
18296−0616	57.8	0.273	0.795	0.056	55.4	0.411	0.831	0.062	970509.2	56.6		
18304−0506	66.0	0.183	0.708	0.040	71.4	0.199	0.548	0.049	030512.0	68.7		
18305−0447	67.0	0.339	0.668	0.048	66.6	0.279	0.646	0.053	020222.4	66.8		
18305−0809	—	—	—	0.067	91.0	0.361	0.624	0.070	020520.0	91.0		
18308−0433	−10.7	0.228	0.021	0.055	−9.8	0.279	0.661	0.081	030514.2	−10.3		
18320−3502	4.5	0.542	2.581	0.065	5.9	0.566	1.548	0.078	021213.5	5.2		
18332−0655	96.1	0.352	1.401	0.073	97.5	0.494	1.631	0.090	970130.6	96.8		y[15]
18335−0603	105.3	0.209	0.879	0.039	102.8	0.229	0.623	0.046	970427.3	104.1		
18335−0930	97.4	0.415	1.678	0.062	92.7	0.403	1.713	0.067	020315.2	95.0		
18340−0446	−15.4	0.182	0.384	0.049	−17.8	0.232	0.372	0.059	030512.2	−16.6		
18340−0648	54.9	0.324	0.410	0.040	52.4	0.258	0.945	0.046	970124.3	53.7		
18340−0839	56.0	1.521	5.635	0.126	54.9	3.011	11.636	0.131	020426.2	55.5	y[6]	n[4]
18342−1230	22.9	0.248	0.413	0.068	25.2	0.254	0.948	0.064	020519.2	24.1		y[4]
18343−0624	33.4	0.364	0.747	0.068	33.4	0.304	0.587	0.084	970130.6	33.4		
18344−0850	62.4	1.434	5.665	0.138	64.4	0.912	4.556	0.142	020315.2	63.4		y[17]
18352−0557	25.7	0.958	1.574	0.102	25.6	0.958	2.263	0.108	980406.3	25.6		
18357−1004	52.4	1.071	3.183	0.090	52.1	0.827	2.559	0.091	020523.1	52.3		
18364−0710	76.3	0.541	0.901	0.067	76.1	0.349	0.491	0.092	030514.2	76.2		
18366−0322	1.4	2.059	6.778	0.141	1.4	2.607	7.873	0.126	970525.1	1.4		
18367−0507	80.4	0.631	2.912	0.101	82.8	0.619	2.871	0.132	030519.2	81.6	y[14]	
18370−0004	37.3	1.975	12.571	0.179	36.7	1.794	4.989	0.235	030516.3	37.0		
18373−0509	32.4	0.394	2.591	0.060	31.7	0.215	1.061	0.052	980423.3	32.0		
18376−0505	91.1	0.482	1.072	0.089	90.8	0.775	1.249	0.097	970510.2	90.9		y[17]
18379−0528	29.6	0.182	1.127	0.036	29.9	0.111	0.316	0.035	990412.3	29.8		
18380−0623	15.8	0.124	0.353	0.026	16.5	0.169	0.633	0.030	970526.9	16.1		
18383−0357	117.1	0.205	0.513	0.035	115.7	0.165	0.545	0.045	980507.2	116.4		
18384−0553	40.2	0.243	0.845	0.053	40.3	0.350	1.038	0.055	970126.6	40.2		
18385−0617	72.0	5.158	10.694	0.728	71.8	5.087	12.073	0.772	010524.1	71.9	y[16]	y[17]
18386−0624	45.8	3.719	12.236	0.124	47.1	3.686	15.106	0.126	010523.1	46.5		
18386−0734	1.9	0.356	0.891	0.083	2.0	0.498	1.225	0.108	030519.2	2.0		y[4]
18391+0004	98.2	0.164	0.540	0.036	98.5	0.254	0.679	0.045	980605.2	98.4		
18392−0442	147.1	0.201	0.197	0.049	147.2	0.199	0.344	0.057	970509.2	147.1		
18393−0258	65.5	0.153	0.373	0.039	66.1	0.175	0.894	0.044	970127.3	65.8		

Table 1. (Continued)

	SiO $v=1$, $J=1$–0				SiO $v=2$, $J=1$–0						Prev.	Obs.
IRAS name	V_{peak}	T_{peak}	$Flux$	RMS	V_{peak}	T_{peak}	$Flux$	RMS	Obs.Date	V_{ave}	SiO	OH
	(km s^{-1})	(K)	(K km s^{-1})	(K)	(km s^{-1})	(K)	(K km s^{-1})	(K)	(yymmdd.d)	(km s^{-1})		
18393−1020	−74.7	0.282	0.501	0.084	−74.7	0.600	0.753	0.085	010523.1	−74.7		
18401−0323	30.3	1.266	7.515	0.143	29.7	0.711	3.840	0.097	970523.9	30.0		
18402−0458	168.4	0.227	0.644	0.044	171.7	0.241	0.698	0.041	970423.3	170.1		
18408−0547	75.4	1.153	1.699	0.135	75.3	0.822	1.509	0.115	010525.1	75.3		
18410−0647	79.1	0.300	0.454	0.057	81.8	0.277	1.027	0.057	010523.1	80.4		
18411−0507	101.6	0.141	0.135	0.053	102.5	0.320	0.562	0.048	970523.9	102.1		
18412−0509	98.8	0.618	1.674	0.081	99.2	0.595	2.030	0.079	970526.9	99.0		
18417−0103	48.5	1.603	5.169	0.117	48.3	0.893	3.770	0.119	020315.3	48.4		
18417−0200	64.0	0.104	0.226	0.033	68.3	0.188	0.018	0.037	980420.4	66.1		
18417−0205	60.1	0.101	0.247	0.024	60.7	0.178	0.119	0.027	980420.3	60.4		
18418+0204	19.2	0.536	2.376	0.089	19.1	0.943	2.736	0.122	030516.0	19.2		n[18]
18422+0104	64.4	0.518	1.519	0.073	64.7	0.444	1.156	0.096	030526.1	64.6		
18422−0116	45.5	0.715	2.064	0.106	46.0	0.880	2.595	0.125	980408.4	45.8		
18422−0437	115.6	0.357	0.459	0.106	113.0	0.470	0.918	0.098	970126.6	114.3		
18425−0736	79.4	0.287	0.969	0.068	78.9	0.271	0.795	0.065	010523.1	79.2		y[7]
18426−0352	71.7	0.415	1.786	0.082	73.5	0.443	1.012	0.083	970525.9	72.6		
18429−0814	47.3	0.650	1.542	0.086	46.9	0.554	1.324	0.081	010523.1	47.1		
18431−0403	45.8	1.630	3.504	0.089	46.2	1.116	3.008	0.098	020602.1	46.0	y[16]	y[17]
18432−0040	61.1	0.385	0.629	0.053	59.9	0.447	0.917	0.058	990426.2	60.5		
18432−0428	32.8	0.198	0.676	0.041	31.6	0.176	0.507	0.048	980531.2	32.2		
18446−0034	100.3	0.331	1.556	0.065	103.5	0.377	0.906	0.069	980421.3	101.9		
18446−0706	130.6	0.245	0.982	0.044	127.8	0.254	0.780	0.052	970127.2	129.2		
18447−0741	18.4	0.236	0.837	0.040	22.0	0.172	0.605	0.038	970127.2	20.2		
18449−0514	86.7	0.468	0.587	0.140	86.9	0.486	1.483	0.090	970509.0	86.8		y[17]
18453−0348	118.4	0.424	0.628	0.069	118.1	0.333	0.735	0.077	990415.3	118.3		
18457−0323	87.5	0.278	1.018	0.046	87.5	0.310	1.055	0.055	970127.3	87.5		
18470+0157	46.0	0.158	0.797	0.032	46.8	0.313	1.047	0.037	990528.2	46.4		
18473−0326	118.1	0.157	0.261	0.029	118.4	0.123	0.303	0.034	020222.2	118.3		
18474+0150	42.0	0.133	0.246	0.029	40.3	0.155	0.384	0.041	990427.3	41.2		
18477+0243	121.8	0.230	0.287	0.054	121.6	0.488	0.651	0.066	020521.2	121.7		y[4]
18478−0058	70.6	0.658	1.340	0.084	70.7	0.758	2.215	0.086	980407.4	70.7		
18480−0131	113.2	0.135	0.374	0.036	114.5	0.141	0.318	0.043	000425.3	113.8		
18481−0216	59.6	0.120	0.449	0.032	62.1	0.208	0.645	0.034	990522.2	60.8		
18481−0346	14.8	0.626	1.661	0.111	15.1	0.781	0.988	0.130	970126.6	15.0		
18485+0010	48.9	0.676	1.908	0.053	48.6	0.325	1.173	0.072	030529.0	48.7		
18485+0028	47.8	0.234	0.939	0.064	48.2	0.268	1.437	0.062	010525.0	48.0		
18487+0152	27.3	2.458	4.724	0.183	27.3	2.293	6.564	0.175	980408.4	27.3		y[17]
18490+0302	131.4	0.711	1.490	0.089	131.3	0.749	2.125	0.098	030529.0	131.3		y[4]
18494−0130	—	—	—	0.177	76.7	0.970	2.072	0.180	980409.4	76.7	y[16]	y[17]
18498−0221	—	—	—	0.050	104.9	0.204	0.066	0.054	020426.2	104.9		
18502−0230	85.7	0.163	0.380	0.033	85.5	0.194	0.237	0.038	000428.2	85.6		
18503−0141	139.7	0.527	0.962	0.107	140.4	0.356	1.254	0.126	980409.4	140.1		
18512+0211	78.1	0.334	1.508	0.057	82.6	0.454	0.923	0.058	020519.3	80.4		
18516+0028	44.6	0.257	0.583	0.041	45.1	0.244	0.955	0.045	990426.1	44.8		
18517+0312	−6.1	0.417	0.814	0.058	−5.9	0.259	0.581	0.055	990509.2	−6.0		
18522+0021	101.3	0.433	4.508	0.073	—	—	—	—	030516.3	101.3		
18530+0507	—	—	—	0.035	17.8	0.133	0.445	0.037	990512.0	17.8		y[18]
18544+0150	10.2	0.287	1.171	0.044	14.0	0.127	0.388	0.044	990425.2	12.1		
18547−0112	125.2	0.195	0.512	0.046	124.5	0.288	0.494	0.051	980531.2	124.9		
18550+0104	73.8	0.415	1.853	0.067	73.9	0.513	1.957	0.072	980426.4	73.8		
18550+0130	36.3	0.638	3.430	0.098	39.8	0.435	2.452	0.089	990414.4	38.1	y[6]	n[4]
18552−0119	48.5	0.103	0.242	0.025	48.7	0.163	0.393	0.030	980608.1	48.6		y[4]
18554+0231	12.6	1.635	3.428	0.145	12.7	1.492	2.796	0.130	990426.1	12.6		y[7]
18554+0402	25.4	0.246	0.592	0.050	24.1	0.260	0.875	0.054	990508.2	24.8		
18556+0053	101.9	0.285	0.780	0.047	107.0	0.152	0.593	0.052	000427.3	104.5		
18559+0510	60.5	0.640	2.140	0.070	60.6	0.714	2.379	0.068	990424.3	60.5		
18560+0638	20.6	12.649	33.483	0.672	20.6	18.787	63.496	0.172	990426.1	20.6	y[19]	y[17]
18564+0155	69.2	0.352	1.711	0.062	67.5	0.273	0.702	0.057	990510.2	68.4		
18564+0232	80.7	0.440	0.314	0.078	80.2	0.654	0.981	0.084	020519.3	80.4		y[20]

Table 1. (Continued)

IRAS name	SiO $v=1$, $J=1$–0				SiO $v=2$, $J=1$–0				Obs.Date	V_{ave}	Prev.	Obs.
	V_{peak}	T_{peak}	$Flux$	RMS	V_{peak}	T_{peak}	$Flux$	RMS			SiO	OH
	(km s^{-1})	(K)	(K km s^{-1})	(K)	(km s^{-1})	(K)	(K km s^{-1})	(K)	(yymmdd.d)	(km s^{-1})		
18574+0812	36.5	0.445	2.395	0.102	34.6	0.608	1.248	1.248	030516.2	35.6		
18582−0016	110.2	0.214	0.267	0.039	115.3	0.144	0.317	0.047	980604.2	112.8		
18588+0428	50.9	0.989	7.226	0.122	52.4	1.611	8.995	0.080	990428.3	51.6		y[13]
18595−0053	80.9	0.573	0.991	0.165	80.5	0.850	2.544	0.208	980512.2	80.7		
18596+0605	68.2	0.161	0.632	0.039	64.0	0.166	0.618	0.041	990426.3	66.1		
19010+0526	41.7	0.280	0.938	0.063	41.3	0.480	0.997	0.059	010523.0	41.5	y[6]	y[4]
19010−3110	−60.2	0.801	1.999	0.060	−60.3	0.578	1.893	0.067	021212.6	−60.3		
19017+0412	86.6	1.056	2.191	0.118	86.3	1.382	2.779	0.124	020315.3	86.4		y[21]
19027+0517	33.0	0.442	1.374	0.071	32.7	0.694	1.515	0.071	020520.2	32.9		
19028+0604	23.3	0.849	2.525	0.095	23.8	1.285	4.106	0.096	990425.3	23.5		
19055+0225	19.4	0.562	1.555	0.079	19.4	0.842	1.760	0.086	010525.1	19.4		y[21]
19074+0336	31.4	0.301	0.871	0.057	33.0	0.226	0.606	0.071	990424.3	32.2		y[21]
19093−3256	40.8	2.604	7.473	0.054	40.8	3.890	10.067	0.064	010209.4	40.8	y[3]	n[4]
19160−2948	33.7	0.444	0.615	0.120	—	—	0.132	—	021212.6	33.7		
19240+1634	12.9	1.131	3.591	0.108	13.5	1.127	3.712	0.138	030518.1	13.2		y[20]
19240+1806	26.7	0.595	3.148	0.095	25.6	1.131	3.521	0.135	030518.1	26.2		
19313−3021	45.8	0.611	2.189	0.055	51.8	0.447	0.532	0.063	010209.4	48.8		
19502−2838	−16.6	0.337	0.308	0.083	−16.8	0.328	0.544	0.095	021213.7	−16.7		
20343−3020	−25.5	0.748	2.345	0.053	−25.8	0.987	1.815	0.064	010209.4	−25.6	y[9]	y[4]
20372−3948	−96.6	0.531	2.050	0.056	−96.5	0.551	1.464	0.064	010209.5	−96.6	y[9]	

References: [1]. Jiang et al. 1996, [2] Galt et al. 1989, [3] Haikala et al. 1994, [4] te Lintel-Hekkert et al. 1991, [5] Lewis et al. 1995, [6] Nyman et al. 1998, [7] Le Squeren et al. 1992, [8] NRO pointing source list, [9] Deguchi et al. 2001b, [10] Ita et al. 2001, [11] Lewis 2000, [12] Sivagnanam et al. 1990, [13] Sevenster et al. 1997, [14] Messineo et al. 2002, [15] Blommaert et al. 1994, [16] Jewell et al. 1991, [17] te Lintel-Hekkert et al. 1989, [18], Chengalur et al. 1993, [19] Engels, Heske 1989, [20] Lewis 1994, [21] Eder et al. 1988, [22] Jiang et al. 1999, [23] Alcolea et al. 1990

Table 2. List of nagtive results

IRAS name	$v=1$ rms (K)	$v=2$ rms (K)	Obs.date (*yymmdd.d*)
13466−3512	0.062	0.069	010410.0
15191−3905	0.087	0.092	010410.0
15589−2850	0.103	0.088	030526.0
16039−2040	0.168	0.135	030521.0
16275−2638	0.124	0.091	030523.0
16281−2433	0.086	0.072	030528.0
16342−3814	0.066	0.072	010410.0
16372−2347	0.081	0.070	030525.0
16423−2309	0.092	0.070	030529.0
16593−2338	0.122	0.095	030528.0
17215−3336	0.072	0.069	020604.0
17265−0725	0.139	0.108	030521.0
17279−3042	0.105	0.111	021213.5
17279−3326	0.070	0.072	020531.9
17289−3106	0.041	0.043	020307.2
17309−3412	0.046	0.042	020307.3
17317+0054	0.067	0.054	030527.1
17375−3247	0.060	0.056	020602.0
17379+0157	0.073	0.056	030527.1
17399−0625	0.105	0.080	030521.0
17424−2806	0.088	0.067	030513.0
17490−0226	0.097	0.077	030521.1
17499−2516	0.105	0.093	020602.0
17502−3039	0.101	0.072	030511.0
17535−2801	0.086	0.072	030512.1
17581−2130	0.056	0.057	020531.0
18002−2005	0.095	0.114	030527.0
18013−2333	0.061	0.075	020223.2
18017−1917	0.133	0.190	030516.1
18026−1827	0.110	0.190	030516.1
18033−1551	0.059	0.061	020531.0
18034−2454	0.035	0.038	010310.3
18084−1946	0.078	0.103	030517.0
18089−1953	0.061	0.083	030517.1
18111−2111	0.045	0.042	020426.1
18114−1614	0.062	0.063	020602.1
18120−1417	0.091	0.090	020219.4
18121−1825	0.052	0.051	020426.1
18137−1557	0.108	0.101	020220.4
18142−1527	0.087	0.083	010526.1
18181−1307	0.052	0.052	020531.1
18188−1342	0.052	0.054	010403.1
18205−1212	0.048	0.047	020519.2
18208−1542	0.054	0.052	020531.1
18230−1144	0.064	0.050	030512.2
18237−1153	0.059	0.057	020426.2
18262−1346	0.096	0.063	030511.2
18267−0606	0.081	0.074	990525.0
18275−1315	0.064	0.062	020531.1
18289−0446	0.060	0.078	030517.0
18290−1200	0.100	0.096	020523.2
18294−0400	0.356	0.442	030516.2
18303−0519	0.066	0.062	990525.1
18307−0632	0.124	0.114	970124.6
18310−0603	0.104	0.138	030516.2
18311−0315	0.099	0.135	030519.2
18314−0517	0.049	0.041	980423.3
18316−0542	0.036	0.032	970510.2
18319−0718	0.061	0.054	020313.3
18320−0253	0.081	0.102	030517.0
18320−0352	0.065	0.058	970514.1
18320−0544	0.031	0.029	970526.2
18322−0859	0.080	0.075	020315.3
18330−0408	0.043	0.038	980510.2
18342−0330	0.092	0.072	030516.0
18353−0500	0.046	0.051	990524.2
18353−0820	0.062	0.067	020315.3
18355−0921	0.050	0.046	020313.3
18356−0828	0.066	0.064	020315.2
18361−0427	0.059	0.048	970422.4
18364−0220	0.057	0.049	970127.6
18367−0452	0.058	0.055	020521.2
18367−0630	0.066	0.058	980426.3
18369−0525	0.052	0.047	980511.2
18369−1034	0.082	0.080	020521.2
18370−0614	0.085	0.075	980406.3
18371−2837	0.075	0.085	021213.6
18372−0247	0.064	0.072	970509.1
18373−3651	0.100	0.113	021212.6
18377−0316	0.064	0.061	020315.2
18377−0620	0.044	0.034	980530.2
18378−0651	0.091	0.073	030518.0
18379−0541	0.033	0.031	970523.9
18383−0250	0.026	0.022	980531.2
18386−0162	0.062	0.056	020520.2
18386−0428	0.050	0.044	990412.3
18387−0228	0.048	0.043	970523.0
18390−0547	0.094	0.083	970523.2
18397−0249	0.052	0.046	020222.4
18397−0400	0.066	0.059	970509.2
18404−0645	0.073	0.063	020315.2
18406−0508	0.067	0.062	970514.2
18407−0439	0.052	0.041	030529.0
18418−0025	0.031	0.034	980421.3
18419−0507	0.042	0.042	970514.1
18420−0123	0.032	0.025	980408.3
18420−0316	0.034	0.027	980422.3
18421−0257	0.074	0.061	980406.4
18421−0318	0.093	0.075	980406.4
18424−0509	0.043	0.037	980425.3

Table 2. (Continued)

IRAS name	$v=1$ rms (K)	$v=2$ rms (K)	Obs.date (*yymmdd.d*)
18425−0442	0.050	0.045	970522.9
18425−0607	0.082	0.070	980513.2
18430−0634	0.131	0.122	020315.3
18440−0241	0.161	0.135	980409.3
18440−0613	0.108	0.090	030526.1
18441+0311	0.055	0.051	990414.3
18441−0325	0.103	0.089	970422.4
18443−0446	0.083	0.067	970427.3
18445−0326	0.082	0.071	990523.2
18449+0042	0.078	0.067	980407.3
18463+0053	0.048	0.040	990528.2
18463−0223	0.061	0.048	980513.2
18464−0656	0.082	0.082	010524.0
18470−0115	0.074	0.062	980422.4
18474−0013	0.055	0.046	980425.3
18476+0017	0.078	0.069	980407.4
18479+0432	0.070	0.093	030516.3
18481+0038	0.043	0.036	990426.3
18485+0038	0.104	0.085	980526.2
18487+0617	0.049	0.046	990414.3
18490−0249	0.079	0.063	980930.2
18491+0205	0.044	0.043	990522.2
18499−0021	0.107	0.125	010524.0
18503−2626	0.064	0.047	030522.1
18512−0051	0.048	0.044	980421.4
18520+0058	0.106	0.100	980424.3
18521+0247	0.035	0.033	990509.2
18522+0049	0.049	0.045	990523.2
18526−0029	0.120	0.096	030512.2
18537+0314	0.041	0.031	990424.2
18538+0114	0.116	0.064	980426.3
18545−0148	0.056	0.046	990426.2
18550+0242	0.050	0.046	990414.4
18550+0358	0.033	0.031	990513.2
18551−0218	0.075	0.071	990523.2
18562+0315	0.035	0.031	990508.3
18567+0134	0.032	0.026	990511.2
18567+0358	0.038	0.033	990510.3
18576+0442	0.035	0.030	990512.2
18581+0339	0.042	0.035	990512.2
18596+0315	0.071	0.052	030512.0
18597+0556	0.054	0.044	990526.2
19015+0212	0.042	0.036	990513.3
19018+0222	0.047	0.038	990514.2
19024−3439	0.075	0.070	020218.4
19035−1514	0.078	0.060	030524.1
21046−2407	0.211	0.192	020218.4

Table 3. 2MASS and MSX identification of IRAS sources with SiO masers

IRAS name	MSX5C name	RA(J2000) (∘)	Dec(J2000) (∘)	J (mag)	H (mag)	K (mag)	$Bflag$	D_L (kpc)
14251−3246	—	217.0387	−33.0010	8.680	7.282	5.830	111	2.50
14402−3645	—	220.8292	−36.9689	6.025	5.119	4.421	111	2.87
15060+0947	—	227.1074	9.6051	5.450	4.520	3.836	111	1.12
15576−1212	—	240.0990	−12.3493	5.641	4.552	3.621	111	1.66
16038−2230	—	241.7044	−22.6438	4.978	3.742	3.161	111	1.66
16063−3227	—	242.3742	−32.5914	6.535	5.255	4.325	111	2.62
16091−1655	—	242.9994	−17.0539	5.977	5.103	4.116	111	2.15
16156−2837	—	244.6974	−28.7530	4.475	3.380	2.782	111	1.31
16309−1949	—	248.4778	−19.9314	6.319	5.318	4.693	111	3.34
16322−2205	—	248.7980	−22.1953	5.312	4.043	3.257	111	1.65
16339−2712	—	249.2639	−27.3132	6.038	5.060	4.196	111	2.49
16388−2939	—	250.5079	−29.7531	6.020	4.799	3.872	111	2.39
16473−2528	—	252.6067	−25.5604	5.485	4.581	3.882	111	2.05
16482−2039	—	252.8063	−20.7368	6.399	5.231	4.372	111	2.69
16559−2557	—	254.7520	−26.0308	5.458	4.186	3.463	111	1.73
17100−3521	G350.8356+02.1055	258.3440	−35.4134	10.176	7.798	6.135	111	4.32
17103−0559	—	258.2422	−6.0492	9.229	7.338	5.870	111	1.54
17115−3538	G350.7958+01.6847	258.7347	−35.6915	11.652	9.204	7.447	111	6.11
17122−2019	—	258.8115	−20.3817	5.696	4.459	3.726	111	1.73
17181−1901	—	260.2729	−19.0655	6.540	5.396	4.641	111	3.20
17186−3445	G352.3427+01.0228	260.4874	−34.8076	9.618	7.005	5.284	111	2.92
17197−3517	G352.0439+00.5299	260.7769	−35.3329	14.368	10.834	8.008	111	4.32
17205−1609	—	260.8509	−16.2101	6.729	5.674	4.877	111	3.27
17220−3118	G355.5829+02.3991	261.3116	−31.3568	11.803	9.196	7.417	111	6.12
17232−3620	G351.5661−00.6504	261.6503	−36.3918	15.143	11.624	9.064	120	4.20
17255−2928	G357.5285+02.7955	262.1830	−29.5219	9.353	7.324	6.138	111	5.25
17264−3521	G352.7495−00.6440	262.4540	−35.4034	13.524	11.388	8.382	001	3.38
17269−2625	G000.2460+04.2292	262.5164	−26.4675	8.496	6.995	5.538	111	1.46
17318−2342	G003.1417+04.7995	263.7155	−23.7323	3.354	2.102	1.606	111	0.81
17323−0556	—	263.7650	−5.9670	5.622	4.459	3.596	111	2.04
17352−3252	G355.8304−00.7964	264.6294	−32.8983	7.250	5.203	3.846	111	1.95
17360−3012	G358.1617+00.4902	264.8122	−30.2401	9.872	6.926	4.893	111	1.11
17361−2807	G359.9458+01.5934	264.8307	−28.1433	10.513	7.766	5.859	111	2.80
17367−2319	G004.0615+04.0473	264.9419	−23.3567	5.284	4.174	3.478	111	1.48
17371−2718	G000.7443+01.8401	265.0722	−27.3361	14.238	13.364	11.449	010	5.47
17383−3144	G357.1454−00.7499	265.4095	−31.7594	9.371	6.734	5.137	111	2.86
17388−2450	G003.0287+02.8413	265.4684	−24.8706	11.822	9.022	7.199	111	5.91
17390−3014	G358.4970−00.0801	265.5786	−30.2580	9.430	6.723	5.156	111	2.83
17393−3004	G358.6662−00.0438	265.6459	−30.0950	5.794	3.494	2.330	111	0.80
17398−3016	G358.5493−00.2454	265.7730	−30.3004	13.277	9.158	6.754	111	3.38
17403−0658	—	265.7624	−6.9899	6.962	5.542	4.543	111	2.94
17406−2614	G002.0765+01.7380	265.9561	−26.2578	14.077	11.152	8.687	100	6.03
17412−2706	G001.3999+01.1671	266.1051	−27.1329	13.360	9.499	7.175	111	5.64
17413−2508	G003.0862+02.1858	266.1184	−25.1637	12.147	9.886	8.207	111	5.13
17414−2531	G002.7659+01.9816	266.1266	−25.5430	10.850	8.529	7.115	111	6.04
17423−0511	—	266.2609	−5.2102	5.205	4.194	3.615	111	2.03
17424−2622	G002.1567+01.3351	266.3868	−26.3997	10.756	8.444	6.749	111	4.91
17426−2535	G002.8521+01.7136	266.4300	−25.6090	14.359	11.331	8.624	011	6.51
17434−2354	G004.3854+02.4239	266.6373	−23.9312	9.930	7.931	6.342	111	5.42
17443−2519	G003.2884+01.5193	266.8645	−25.3373	14.739	11.504	8.876	011	2.64
17451−2731	G001.4927+00.2141	267.0764	−27.5487	8.564	6.052	4.656	111	2.70
17459−3057	G358.6556−01.7102	267.2910	−30.9716	7.187	5.432	4.279	111	1.87
17465−0731	—	267.3139	−7.5463	9.873	7.929	6.552	111	5.64
17468−2932	G359.9656−01.1443	267.5077	−29.5571	10.891	8.128	6.160	111	3.16
17471−0525	—	267.4515	−5.4453	6.177	5.131	4.347	111	2.78
17473−2549	G003.2072+00.6744	267.6212	−25.8416	12.999	10.604	8.848	111	5.83
17487−2537	G003.5424+00.5225	267.9565	−25.6316	11.050	9.060	7.409	111	3.20
17488−2450	G004.2269+00.9083	267.9751	−24.8461	12.449	9.370	7.519	220	5.73
17488−2532	G003.6212+00.5456	267.9789	−25.5520	9.576	7.132	5.601	111	2.96
17489−2207	G006.5649+02.2699	267.9958	−22.1410	9.537	7.222	5.738	111	4.23

Table 3. (Continued)

IRAS name	MSX5C name	RA(J2000) (○)	Dec(J2000) (○)	J (mag)	H (mag)	K (mag)	$Bflag$	D_L (kpc)
17490−2711	G002.2335−00.3360	268.0362	−27.1948	11.307	7.992	5.977	111	3.70
17493−2139	G007.0126+02.4450	268.0786	−21.6667	10.952	8.806	7.191	111	4.02
17504−2149	G006.9995+02.1244	268.3690	−21.8407	9.403	7.400	6.112	111	5.06
17505−3143	G358.4972−02.9527	268.4478	−31.7406	15.859	14.872	10.655	001	2.45
17515−2747	G001.9916−01.1301	268.6693	−27.8059	14.847	12.914	9.857	011	5.18
17525−2506	G004.4171+00.0439	268.9064	−25.1192	14.578†	11.452†	10.090†	111	4.25
17535−2421	G005.1756+00.2335	269.1436	−24.3695	17.185	15.540	12.166	001	5.73
17536−1950	G009.0863+02.5001	269.1457	−19.8502	5.989	4.815	4.075	111	2.39
17538−2329	G005.9680+00.6160	269.2171	−23.4921	13.547	10.005	7.688	220	3.36
17540−2856	G001.2869−02.1880	269.3058	−28.9472	10.547	8.879	7.614	211	5.40
17548−2652	G003.1722−01.3046	269.5063	−26.8737	10.168	7.713	6.282	111	4.52
17559−2848	G001.6038−02.4805	269.7758	−28.8185	11.062	8.639	7.103	300	2.84
17573−2259	G006.7997+00.1693	270.0903	−22.9946	9.303	7.000	5.530	111	3.00
17575−2644	G003.5691−01.7426	270.1534	−26.7474	8.010	5.885	4.502	111	2.44
17581−1910	G010.1952+01.9092	270.2744	−19.1836	10.945	8.856	7.258	111	5.51
17586−2152	G007.9250+00.4604	270.4201	−21.8727	9.392	6.997	5.617	111	3.69
17591−1829	G010.9053+02.0541	270.5117	−18.4950	9.781	7.424	5.811	111	4.23
17594−2201	G007.8847+00.2392	270.6057	−22.0169	16.129	11.333	8.088	011	4.05
17596−1944	G009.8837+01.3153	270.6591	−19.7478	9.578	7.160	5.456	111	3.08
17599−2603	G004.4403−01.8761	270.7627	−26.0564	10.596	7.872	6.163	111	4.48
18002−2154	G008.0764+00.1329	270.8072	−21.9029	11.543	8.780	7.067	111	3.47
18007−1833	G011.0556+01.6815	270.9318	−18.5475	7.992	6.437	5.323	111	3.58
18008−2701	G003.7077−02.5373	271.0051	−27.0187	11.812	9.902	8.328	111	6.70
18009−1830	G011.1032+01.6718	270.9654	−18.5108	12.907	9.963	7.815	111	5.16
18013−2700	G003.7647−02.6158	271.1129	−27.0074	10.190	8.350	6.797	111	5.63
18020−1820	G011.3782+01.5353	271.2327	−18.3382	14.143	11.050	7.792	011	4.56
18021−1653	G012.6581+02.2099	271.2715	−16.8925	7.288	5.532	4.542	111	2.90
18022−2656	G003.9194−02.7622	271.3405	−26.9438	12.411	10.478	8.614	200	5.23
18025−2354	G006.5970−01.3232	271.3973	−23.9062	13.492	9.813	7.386	111	5.66
18029−2048	G009.3350+00.1288	271.4738	−20.8083	9.418	6.920	5.250	111	2.79
18032−1859	G010.9691+00.9483	271.5618	−18.9820	5.746	4.541	3.840	111	2.40
18034−2441	G006.0217−01.8802	271.6230	−24.6799	14.743	12.561	9.212	011	3.83
18035−2529	G005.3276−02.3015	271.6573	−25.4910	14.787	12.215	8.966	011	4.33
18036−2049	G009.4124−00.0236	271.6563	−20.8152	16.605	12.652	9.560	011	5.27
18038−1614	G013.4331+02.1885	271.6850	−16.2265	8.324	6.395	5.073	111	2.53
18041−2242	G007.8270−01.0450	271.7854	−22.6965	8.375	6.460	5.255	111	3.32
18048−2309	G007.5117−01.4142	271.9697	−23.1517	8.133	6.202	4.997	111	2.77
18051−1638	G013.2264+01.7145	272.0106	−16.6376	11.748	9.106	7.371	111	5.65
18081−1451	G015.1348+01.9557	272.7503	−14.8509	10.974	8.122	6.373	111	4.71
18096−1645	G013.6466+00.7211	273.1324	−16.7489	11.164	8.305	6.564	111	4.95
18099−1449	G015.3745+01.5944	273.1974	−14.8139	6.767	5.272	4.399	111	2.57
18100−1250	G017.1244+02.5333	273.2104	−12.8291	11.593	8.573	6.802	111	4.09
18108−1654	G013.6658+00.4007	273.4355	−16.8857	10.180	7.369	5.766	111	3.67
18114−1934	G011.4010−01.0193	273.6079	−19.5531	12.713	9.101	6.871	111	5.24
18115−2139	G009.5748−02.0321	273.6280	−21.6412	8.650	6.381	4.742	111	1.82
18118−1615	G014.3460+00.5127	273.6723	−16.2342	14.153	10.863	8.432	111	4.98
18119−2035	G010.5586−01.6207	273.7429	−20.5804	12.412	9.456	7.569	200	5.22
18128−2158	G009.4342−02.4521	273.9546	−21.9647	8.623	6.929	5.692	111	3.63
18129−1620	G014.3940+00.2324	273.9529	−16.3251	9.586	6.996	5.548	111	3.65
18135−1505	G015.5583+00.6964	274.1048	−15.0810	13.102	10.052	7.926	111	5.61
18137−1549	G014.9414+00.3025	274.1601	−15.8109	11.452	8.852	7.144	111	4.72
18139−1937	G011.6372−01.5534	274.2258	−19.6000	11.167	8.466	6.624	111	5.44
18143−2128	G010.0497−02.5218	274.3345	−21.4561	13.380	10.048	7.840	111	5.66
18145−1604	G014.8086+00.0168	274.3557	−16.0634	13.095	9.406	7.178	111	4.44
18146−1709	G013.8808−00.5319	274.4004	−17.1408	13.700	9.547	7.069	111	3.62
18147−0946	G020.3842+02.9835	274.3842	−9.7505	15.986	12.663	10.082	111	5.29
18154−1727	G013.7101−00.8319	274.5924	−17.4331	10.236	7.366	5.615	111	3.16
18156−2121	G010.2911−02.7349	274.6578	−21.3443	12.487	9.529	7.359	111	3.38
18173−1100	G019.5931+01.8420	275.0283	−10.9854	16.637	14.679	11.273	011	5.80
18189−1648	G014.6711−01.2579	275.4595	−16.7871	8.698	6.253	4.847	111	3.09

Table 3. (Continued)

IRAS name	MSX5C name	RA(J2000) (∘)	Dec(J2000) (∘)	J (mag)	H (mag)	K (mag)	$Bflag$	D_L (kpc)
18196−1608	G015.3429−01.0887	275.6324	−16.1144	11.864	8.599	6.490	111	2.87
18198−1342	G017.5080+00.0193	275.6718	−13.6824	11.169	8.458	6.546	111	3.59
18199−1144	G019.2503+00.9401	275.6763	−11.7118	10.842	8.349	6.618	111	4.60
18207−1029	G020.4494+01.3611	275.8698	−10.4557	10.832	8.093	6.128	111	3.37
18207−1221	G018.7975+00.4648	275.8884	−12.3345	9.977	7.604	6.126	111	4.02
18210−1359	G017.3990−00.3838	275.9858	−13.9679	12.158	8.586	6.525	111	4.40
18213−1739	G014.1959−02.1604	276.0614	−17.6293	16.720	14.944	11.196	001	6.03
18216−1552	G015.7940−01.3803	276.1205	−15.8525	13.339	11.657	8.838	001	3.46
18222−1029	G020.6168+01.0239	276.2524	−10.4657	9.789	7.274	5.569	111	3.13
18224−0932	G021.4903+01.4254	276.3060	−9.5060	12.840	9.987	8.112	111	6.38
18227−1205	G019.2699+00.1713	276.3799	−12.0541	10.775	7.718	5.959	111	3.95
18231−1500	G016.7441−01.2979	276.5045	−14.9740	15.148	10.813	7.994	111	5.07
18232−1003	G021.1232+00.9994	276.5147	−10.0290	10.372	7.590	5.855	111	3.35
18235−1038	G020.6453+00.6683	276.5859	−10.6066	16.551	12.680	9.255	011	4.17
18236−1422	G017.3624−01.1147	276.6347	−14.3417	9.416	7.211	5.734	111	3.64
18241−1115	G020.1591+00.2531	276.7292	−11.2298	9.761	7.138	5.662	111	3.44
18245−0552	G024.9563+02.6929	276.7998	−5.8500	10.909	8.539	6.677	111	3.05
18254−1106	G020.4433+00.0333	277.0624	−11.0804	9.767	7.139	5.585	111	3.15
18254−1118	G020.2740−00.0504	277.0579	−11.2693	13.467	9.751	7.135	111	3.38
18260−1142	G019.9867−00.3666	277.2078	−11.6705	10.581	7.928	6.264	111	4.22
18266−1411	G017.8669−01.6677	277.3817	−14.1519	8.245	6.236	5.034	111	2.95
18268−0417	G026.6368+02.9121	277.3849	−4.2593	6.262	4.764	3.935	111	2.35
18296−0616	G025.1993+01.3774	278.0856	−6.2436	14.472	11.497	9.293	111	5.02
18304−0506	G026.3283+01.7617	278.2656	−5.0649	8.720	6.827	5.582	111	3.69
18305−0447	G026.6214+01.8703	278.3045	−4.7546	11.653	8.741	6.784	111	5.38
18305−0809	G023.6368+00.2988	278.3232	−8.1270	13.942	9.523	6.766	111	4.67
18308−0433	G026.8607+01.9146	278.3755	−4.5224	11.905	8.957	7.115	111	5.55
18320−3502	—	278.8557	−35.0063	5.297	4.295	3.724	111	2.10
18332−0655	G025.0454+00.2771	278.9972	−6.8869	17.410	11.999	8.587	011	6.05
18335−0603	G025.8413+00.6255	279.0541	−6.0200	13.931	10.164	7.882	111	7.31
18335−0930	G022.7940−00.9760	279.0761	−9.4620	12.022	8.714	6.713	111	4.76
18340−0446	G027.0475+01.1157	279.1732	−4.7234	11.055	8.274	6.204	111	3.75
18340−0648	G025.2345+00.1762	279.1752	−6.7653	16.761	13.007	9.318	022	3.55
18340−0839	G023.6045−00.6931	279.1983	−8.6125	11.926	7.867	5.275	111	2.09
18342−1230	G020.2068−02.5264	279.2709	−12.4717	13.305	10.156	7.803	111	3.84
18343−0624	G025.6246+00.2846	279.2582	−6.3690	10.479	7.680	6.045	211	4.13
18344−0850	G023.4799−00.8662	279.2960	−8.8025	6.536	4.947	3.996	111	2.06
18352−0557	G026.1397+00.2952	279.4869	−5.9063	15.435	11.938	9.916	111	3.59
18357−1004	G022.5303−01.7208	279.6251	−10.0380	8.355	6.507	5.373	111	3.68
18364−0710	G025.1978−00.5415	279.8006	−7.1275	12.536	8.875	6.980	200	4.33
18366−0322	G028.5772+01.1775	279.8218	−3.3362	6.770	5.051	3.975	111	1.89
18367−0507	G027.0404+00.3605	279.8438	−5.0765	10.253	7.925	6.328	111	4.18
18370−0004	G031.5679+02.6049	279.9193	−0.0241	6.014	4.008	3.074	111	1.66
18373−0509	G027.0837+00.2059	280.0016	−5.1088	13.612	9.502	7.200	111	4.74
18376−0505	G027.1714+00.1764	280.0681	−5.0441	13.270	9.756	7.262	111	4.17
18379−0528	G026.8620−00.0745	280.1504	−5.4342	13.920	9.334	6.978	111	5.20
18380−0623	G026.0624−00.5195	280.1796	−6.3483	14.322	10.741	8.415	111	7.13
18383−0357	G028.2534+00.5404	280.2408	−3.9158	10.683	10.067	8.325	022	7.38
18384−0553	G026.5522−00.3798	280.2802	−5.8494	7.903	5.925	4.725	111	2.78
18385−0617	G026.2092−00.5896	280.3097	−6.2502	15.873	13.283	9.759	001	2.22
18386−0624	G026.1172−00.6647	280.3344	−6.3662	7.116	5.147	3.718	111	1.42
18386−0734	G025.0761−01.1879	280.3242	−7.5315	14.228	9.910	7.261	111	6.11
18391+0004	G031.9314+02.2229	280.4252	0.1240	10.553	8.436	7.024	211	7.12
18392−0442	G027.6980−00.0016	280.4689	−4.6575	11.803	8.405	6.510	111	3.64
18393−0258	G029.2450+00.7770	280.4844	−2.9259	12.333	9.238	7.380	111	7.33
18393−1020	G022.7066−02.6314	280.5298	−10.2971	9.979	8.334	6.934	111	5.61
18401−0323	G028.9670+00.3935	280.6985	−3.3484	13.169	9.163	7.294	200	5.09
18402−0458	G027.5766−00.3475	280.7219	−4.9236	13.759	11.112	9.378	111	4.59
18408−0547	G026.9262−00.8569	280.8783	−5.7344	11.883	9.765	8.052	111	5.56
18410−0647	G026.0630−01.3691	280.9401	−6.7365	9.687	7.645	6.299	111	5.04

Table 3. (Continued)

IRAS name	MSX5C name	RA(J2000) (∘)	Dec(J2000) (∘)	J (mag)	H (mag)	K (mag)	$Bflag$	D_L (kpc)
18411−0507	G027.5570−00.6219	280.9579	−5.0662	12.142	9.453	7.634	111	5.50
18412−0509	G027.5316−00.6570	280.9775	−5.1048	12.334	9.931	7.801	111	5.69
18417−0103	G031.2189+01.1332	281.0697	−1.0072	8.222	6.163	4.890	111	2.24
18417−0200	G030.3792+00.6931	281.0778	−1.9554	15.553	13.717	11.630	001	8.64
18417−0205	G030.3109+00.6593	281.0768	−2.0316	12.951	9.729	7.842	111	8.11
18418+0204	G034.0214+02.5431	281.0918	2.1280	6.693	5.308	4.395	111	2.31
18422+0104	G033.1825+01.9985	281.1949	1.1343	9.031	6.908	5.654	111	4.51
18422−0116	G031.0897+00.9113	281.2080	−1.2233	11.844	8.653	6.704	111	4.61
18422−0437	G028.1282−00.6388	281.2347	−4.5661	12.730	9.251	7.283	200	3.16
18425−0736	G025.5089−02.0660	281.3109	−7.5474	9.181	6.993	5.393	111	3.07
18426−0352	G028.8225−00.3742	281.3169	−3.8278	12.107	8.983	6.996	111	4.84
18429−0814	G024.9817−02.4609	281.4242	−8.1959	11.400	9.298	7.835	111	5.28
18431−0403	G028.7191−00.5783	281.4518	−4.0128	9.125	6.215	4.295	111	1.67
18432−0040	G031.7307+00.9706	281.4479	−0.6263	13.013	9.929	7.770	111	7.35
18432−0428	G028.3651−00.7830	281.4724	−4.4214	12.322	9.765	7.993	111	7.36
18446−0034	G032.0007+00.6973	281.8144	−0.5110	10.715	8.131	6.651	111	5.69
18446−0706	G026.1985−02.3119	281.8477	−7.0454	9.917	8.233	7.064	111	6.95
18447−0741	G025.6821−02.6025	281.8727	−7.6378	8.218	6.783	5.900	111	5.32
18449−0514	G027.8825−01.5178	281.9072	−5.1854	14.001	10.836	8.123	111	3.16
18453−0348	G029.1965−00.9366	281.9897	−3.7511	10.661	8.237	6.832	211	6.74
18457−0323	G029.6184−00.8524	282.1068	−3.3375	14.069	10.524	8.389	111	8.88
18470+0157	G034.5216+01.3268	282.4031	2.0198	9.484	7.545	6.323	111	5.93
18473−0326	G029.7551−01.2270	282.5035	−3.3864	11.279	8.763	7.039	111	5.59
18474+0150	G034.4589+01.2002	282.4874	1.9061	11.124	8.290	6.527	111	6.36
18477+0243	G035.2742+01.5406	282.5558	2.7868	9.805	7.620	6.180	111	4.09
18478−0058	G031.9927−00.1821	282.5936	−0.9191	14.779	12.419	8.805	011	2.60
18480−0131	G031.5354−00.4850	282.6548	−1.4643	10.513	7.662	6.071	111	4.96
18481−0216	G030.8866−00.8491	282.6832	−2.2074	15.136	11.031	8.459	111	7.26
18481−0346	G029.5504−01.5463	282.6948	−3.7142	9.775	7.271	5.571	111	2.94
18485+0010	G033.1143+00.1750	282.7870	0.2422	9.224	6.882	5.507	111	3.38
18485+0028	G033.3780+00.3170	282.7808	0.5414	13.080	11.475	8.086	020	5.51
18487+0152	G034.6378+00.9222	282.8165	1.9388	16.255	10.942	7.553	111	2.83
18490+0302	G035.7079+01.3778	282.8985	3.0989	12.478	9.130	6.935	111	5.90
18494−0130	G031.7114−00.7898	283.0060	−1.4462	8.846	6.528	5.050	111	3.15
18498−0221	G030.9978−01.2597	283.1005	−2.2949	15.701	13.198	12.396	100	5.45
18502−0230	G030.9192−01.4316	283.2169	−2.4438	13.746	10.595	8.491	111	8.80
18503−0141	G031.6487−01.0823	283.2382	−1.6352	14.302	11.575	8.866	011	3.97
18512+0211	G035.2151+00.5013	283.4548	2.2607	15.070	10.707	7.938	111	5.28
18516+0028	G033.7299−00.3648	283.5481	0.5437	16.658	11.910	9.014	111	6.53
18517+0312	G036.1591+00.8730	283.5557	3.2694	14.575	12.367	8.788	110	9.87
18522+0021	G033.6915−00.5524	283.6976	0.4240	5.633	3.718	2.864	111	1.28
18530+0507	G038.0183+01.4646	283.8759	5.1946	13.007	9.291	6.992	111	4.41
18544+0150	G035.2548−00.3518	284.2322	1.9065	12.576	8.495	6.371	111	4.83
18547−0112	G032.5911−01.8264	284.3301	−1.1357	14.402	11.295	9.166	111	6.85
18550+0104	G034.6467−00.8560	284.4038	1.1356	12.824	9.044	6.650	111	4.31
18550+0130	G035.0366−00.6397	284.3888	1.5812	11.268	7.770	5.603	111	2.14
18552−0119	G032.5351−01.9927	284.4522	−1.2612	15.578	13.391	10.166	011	7.58
18554+0231	G035.9769−00.2664	284.4864	2.5880	8.704	5.793	4.172	111	1.82
18554+0402	G037.3276+00.4435	284.4719	4.1136	17.221	14.063	10.974	011	7.01
18556+0053	G034.5538−01.0517	284.5358	0.9633	15.912	12.799	10.027	011	9.56
18559+0510	G038.3914+00.8379	284.6071	5.2416	13.696	10.356	8.081	111	4.62
18560+0638	G039.7125+01.4946	284.6254	6.7161	13.169	8.966	5.862	111	0.99
18564+0155	G035.5620−00.7714	284.7462	1.9883	12.024	8.818	7.041	111	5.44
18564+0232	G036.1214−00.4827	284.7450	2.6177	17.696	14.750	11.332	011	5.71
18574+0812	G041.2585+01.9093	284.9642	8.2797	6.097	4.765	3.982	111	2.23
18582−0016	G033.8217−02.1747	285.2008	−0.2001	9.915	8.237	6.933	111	6.82
18588+0428	G038.1012−00.1251	285.3336	4.5421	17.304	11.859	8.566	011	4.21
18595−0053	G033.4093−02.7465	285.5212	−0.8274	11.778	8.821	6.772	111	4.47
18596+0605	G039.6326+00.4549	285.5196	6.1693	12.080	8.973	7.094	111	5.30
19010+0526	G039.2285−00.1670	285.8895	5.5251	14.948	10.084	6.913	121	2.41

Table 3. (Continued)

IRAS name	MSX5C name	RA(J2000) (∘)	Dec(J2000) (∘)	J (mag)	H (mag)	K (mag)	$Bflag$	D_L (kpc)
19010−3110	—	286.0576	−31.0933	5.196	4.145	3.573	111	1.94
19017+0412	G038.2026−00.8881	286.0601	4.2832	16.037	11.276	8.092	011	3.58
19027+0517	G039.2776−00.6123	286.3095	5.3645	13.026	10.238	8.199	111	4.02
19028+0604	G039.9826−00.2758	286.3346	6.1451	15.042	10.455	7.563	111	5.29
19055+0225	G037.0617−02.5474	287.0132	2.5084	13.621	10.782	8.862	210	5.55
19074+0336	G038.3267−02.4172	287.4789	3.6909	11.728	9.305	7.772	111	5.85
19093−3256	—	288.1502	−32.8499	2.099	1.040	0.471	111	0.46
19160−2948	—	289.7899	−29.7217	8.227	7.257	6.545	111	6.78
19240+1634	G051.6924+00.0909	291.5796	16.6756	5.275	4.155	3.195	111	1.49
19240+1806	G053.0333+00.8254	291.5709	18.2043	4.972	3.745	2.874	111	1.37
19313−3021	—	293.6160	−30.2432	5.778	4.615	3.691	111	2.13
19502−2838	—	298.3410	−28.5108	6.413	5.524	4.998	111	3.40
20343−3020	—	309.3456	−30.1739	5.130	4.046	3.444	111	0.53
20372−3948	—	310.1244	−39.6284	5.635	4.856	4.293	111	1.81

† indicates that the identification is uncertain.

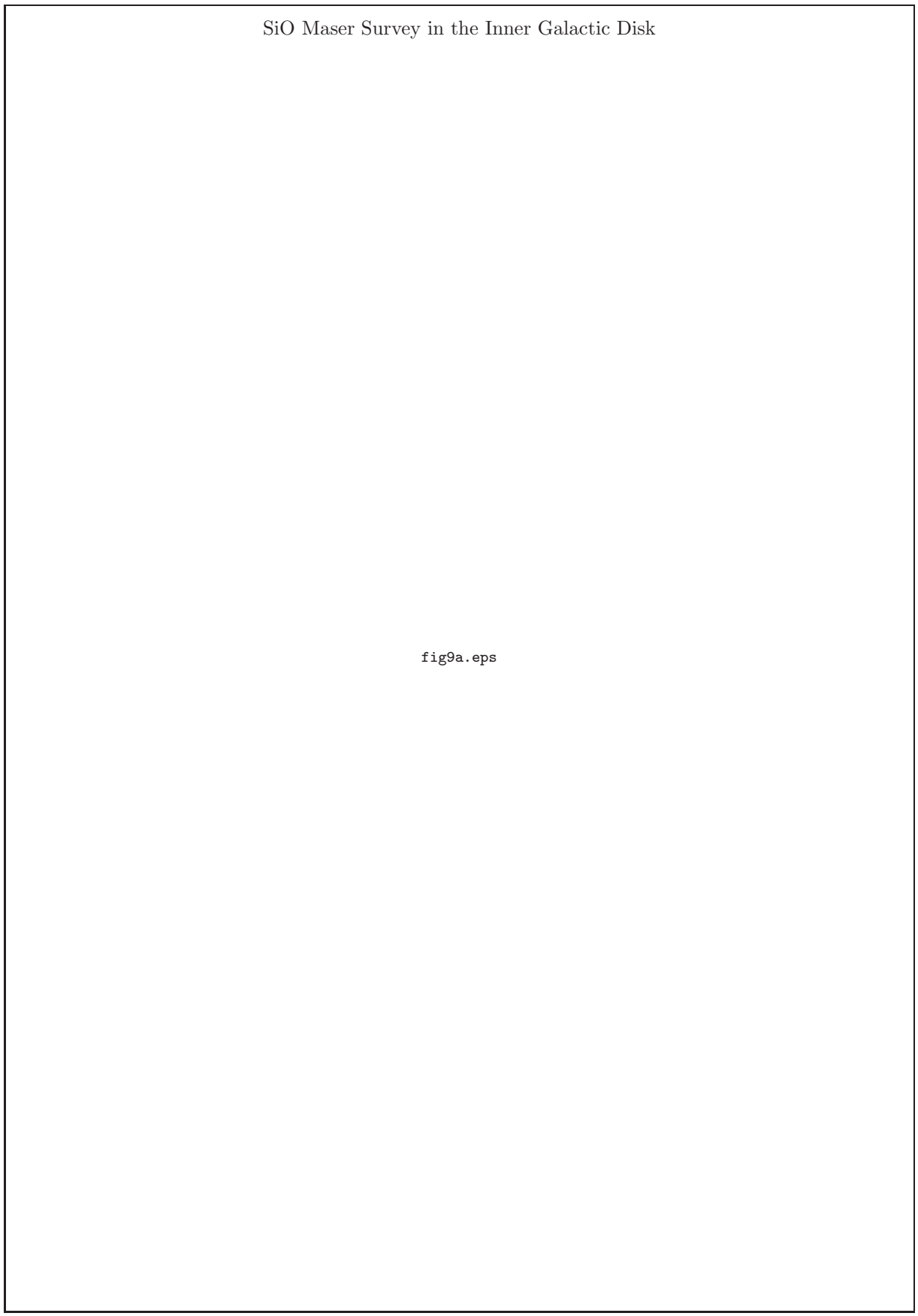

Fig. 9. a – p. SiO $J = 1$–0 $v = 1$ and 2 spectra for the detected sources.

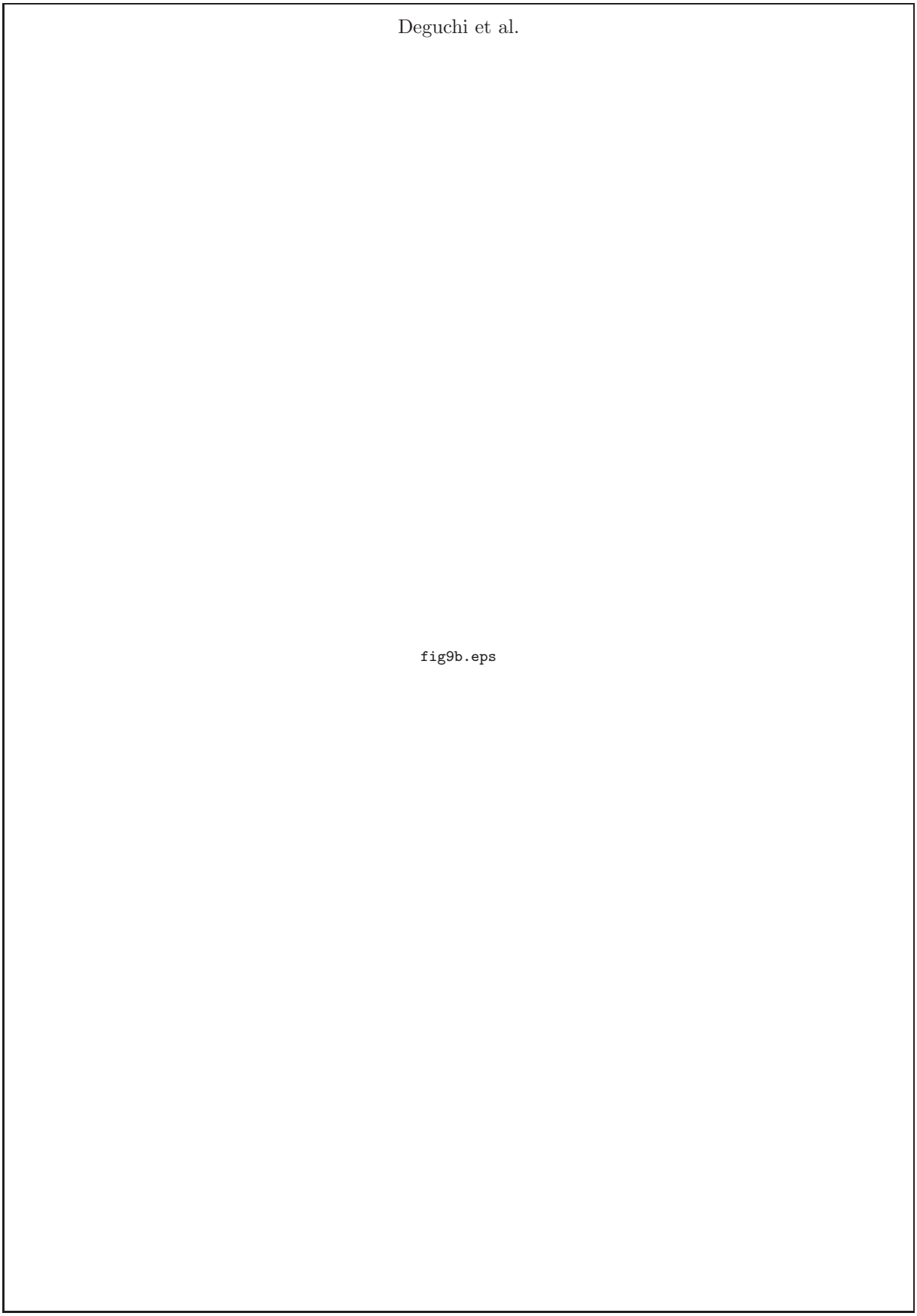

Fig. 9. b.

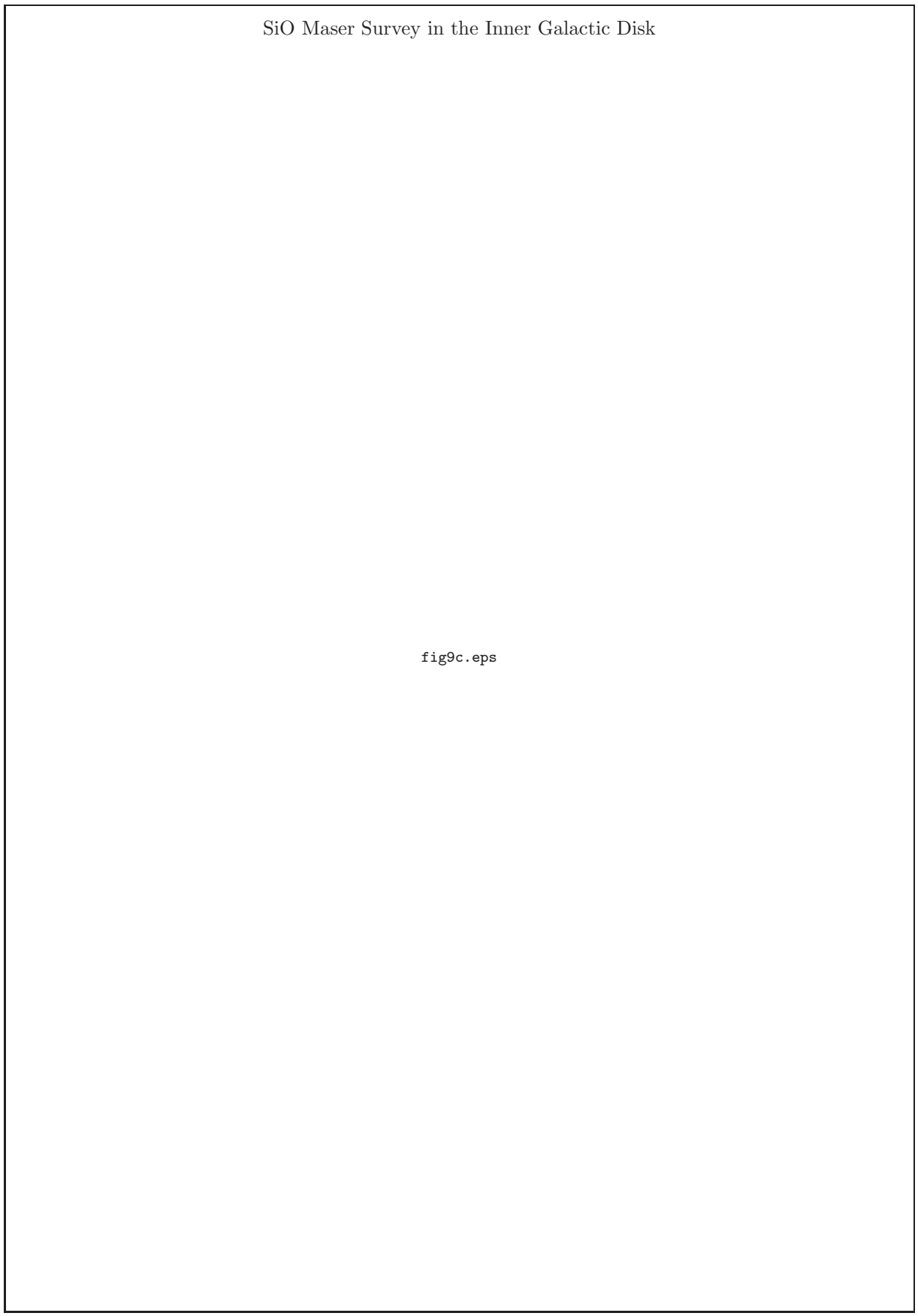

Fig. 9. c.

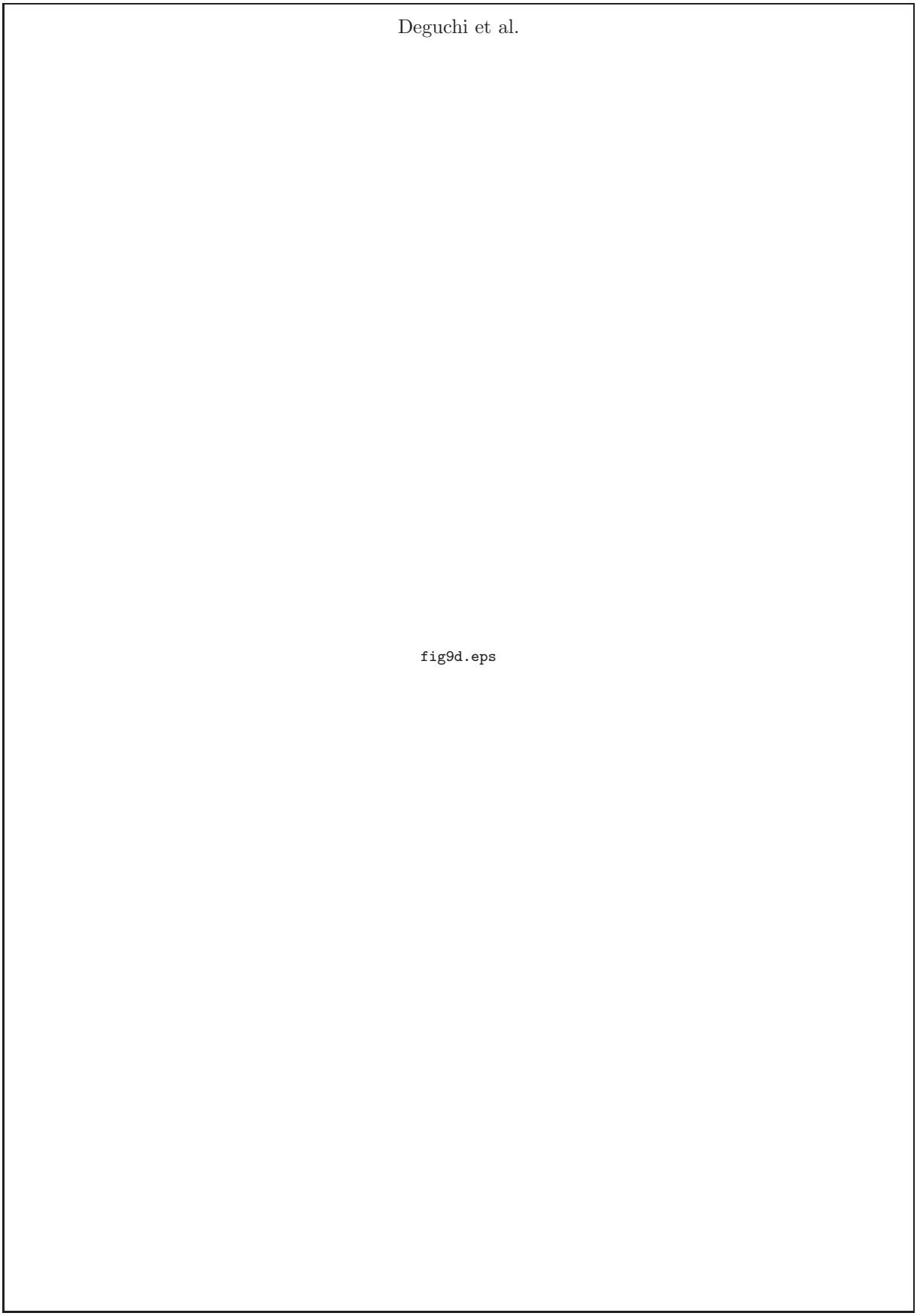

Fig. 9. d.

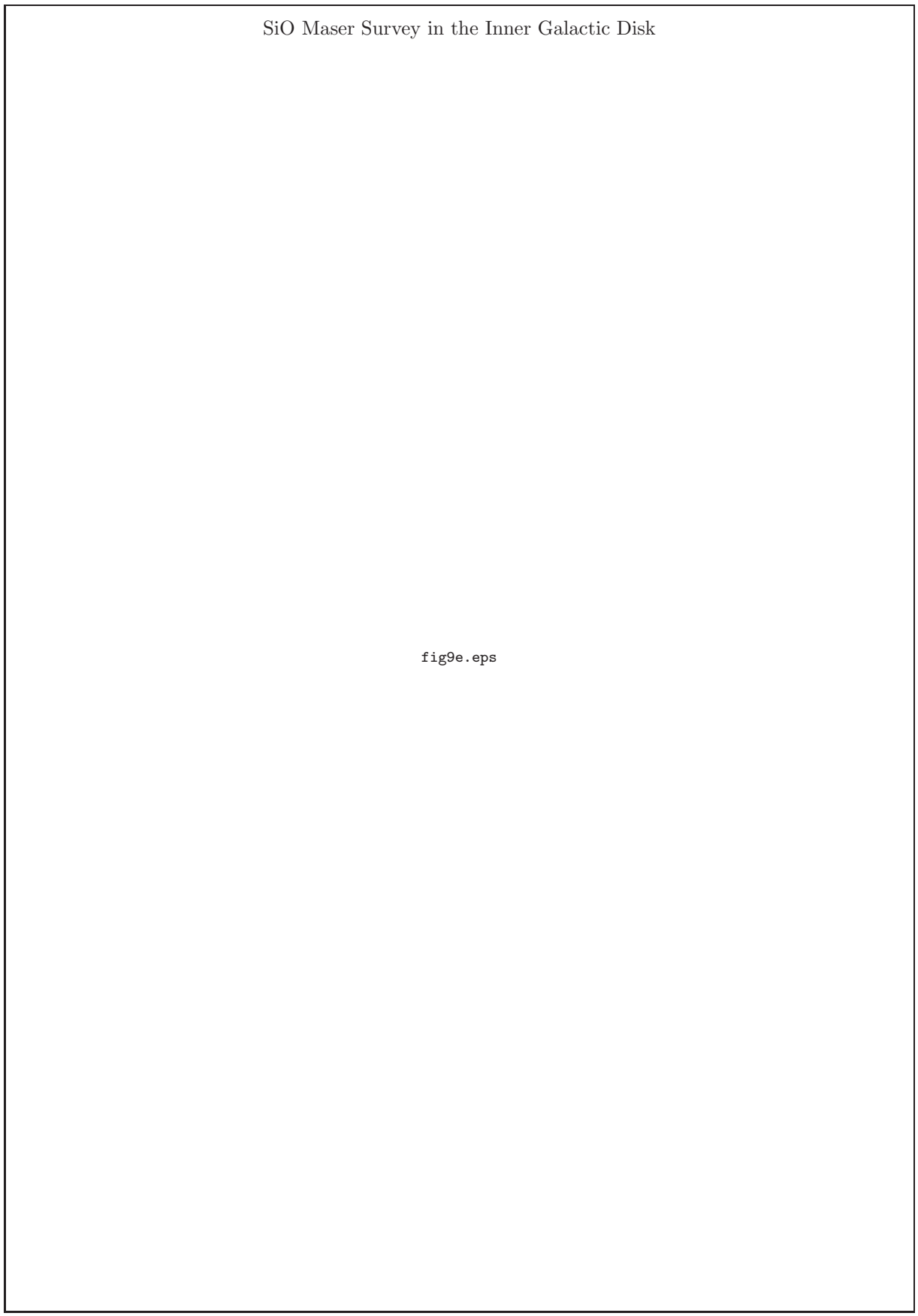

Fig. 9. e.

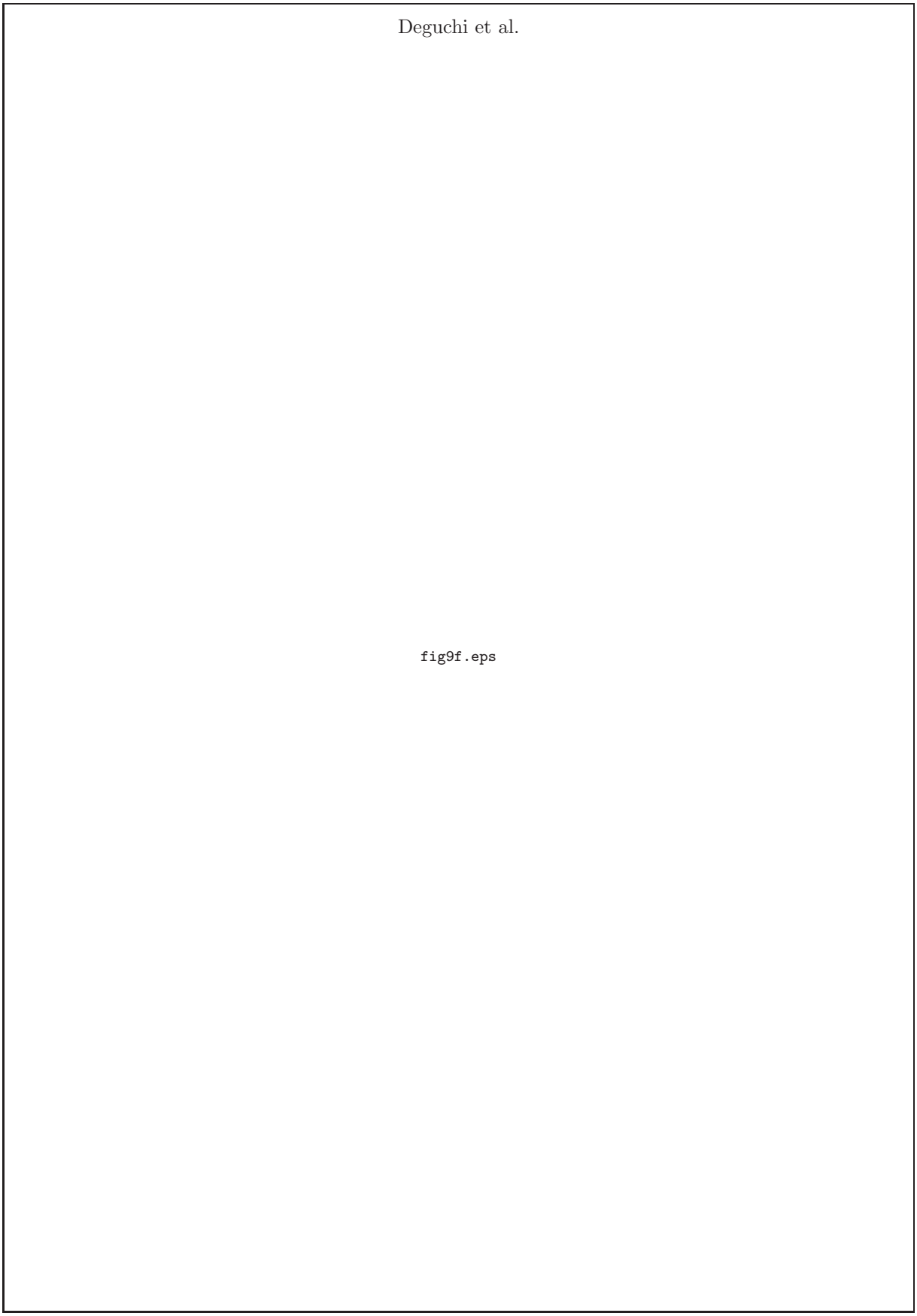

Fig. 9. f.

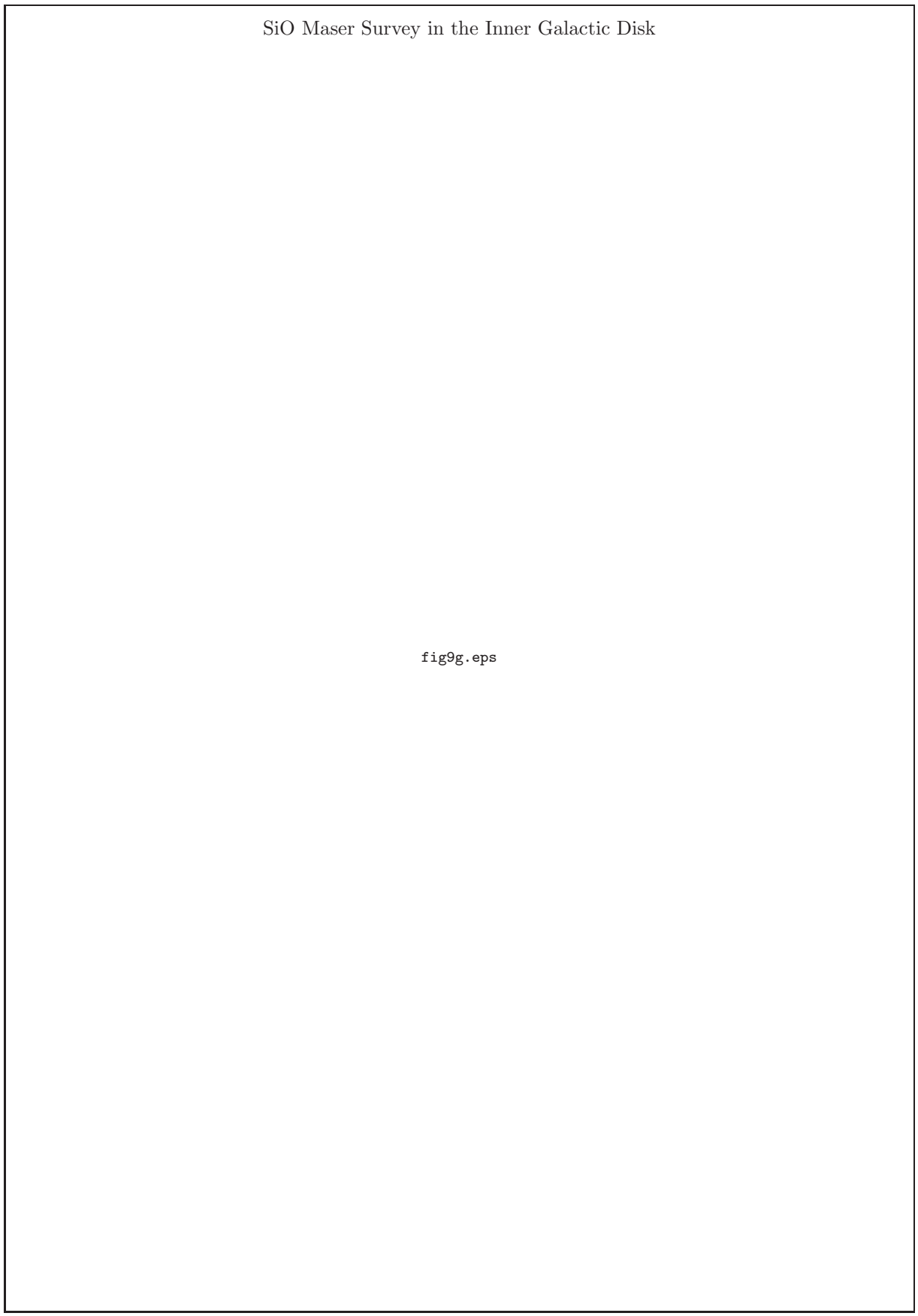

Fig. 9. g.

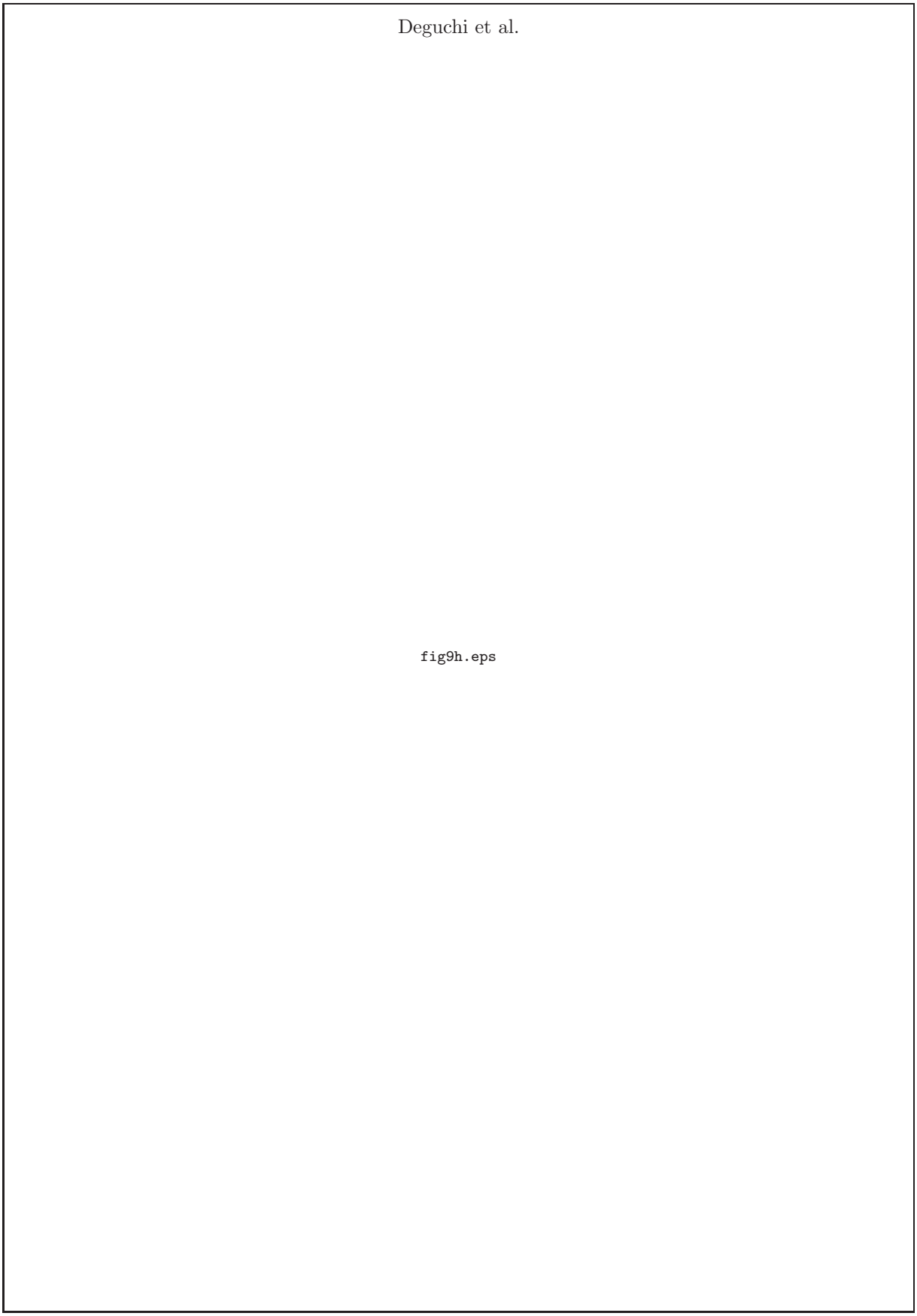

Fig. 9. h.

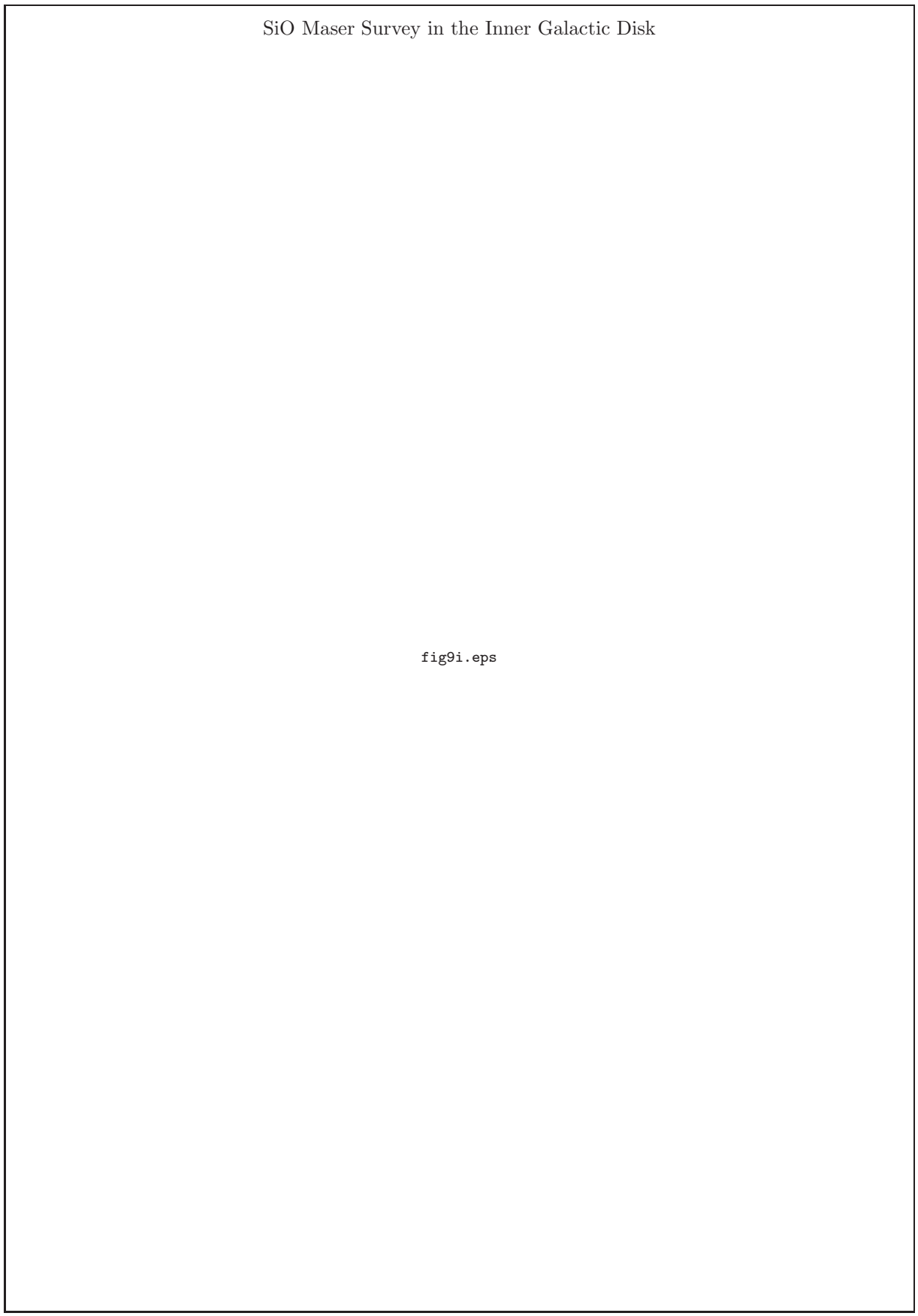

Fig. 9. i.

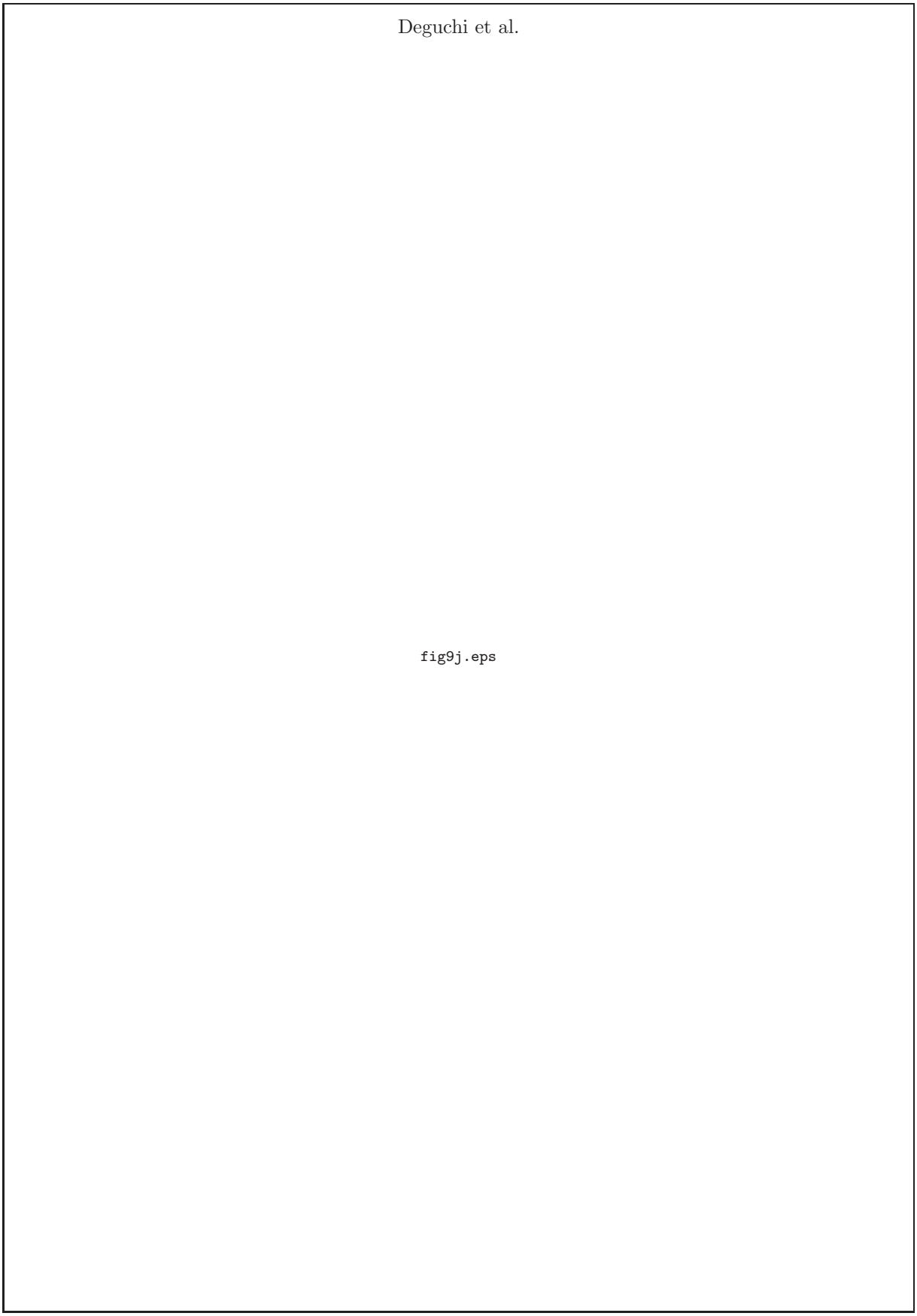

Fig. 9. j.

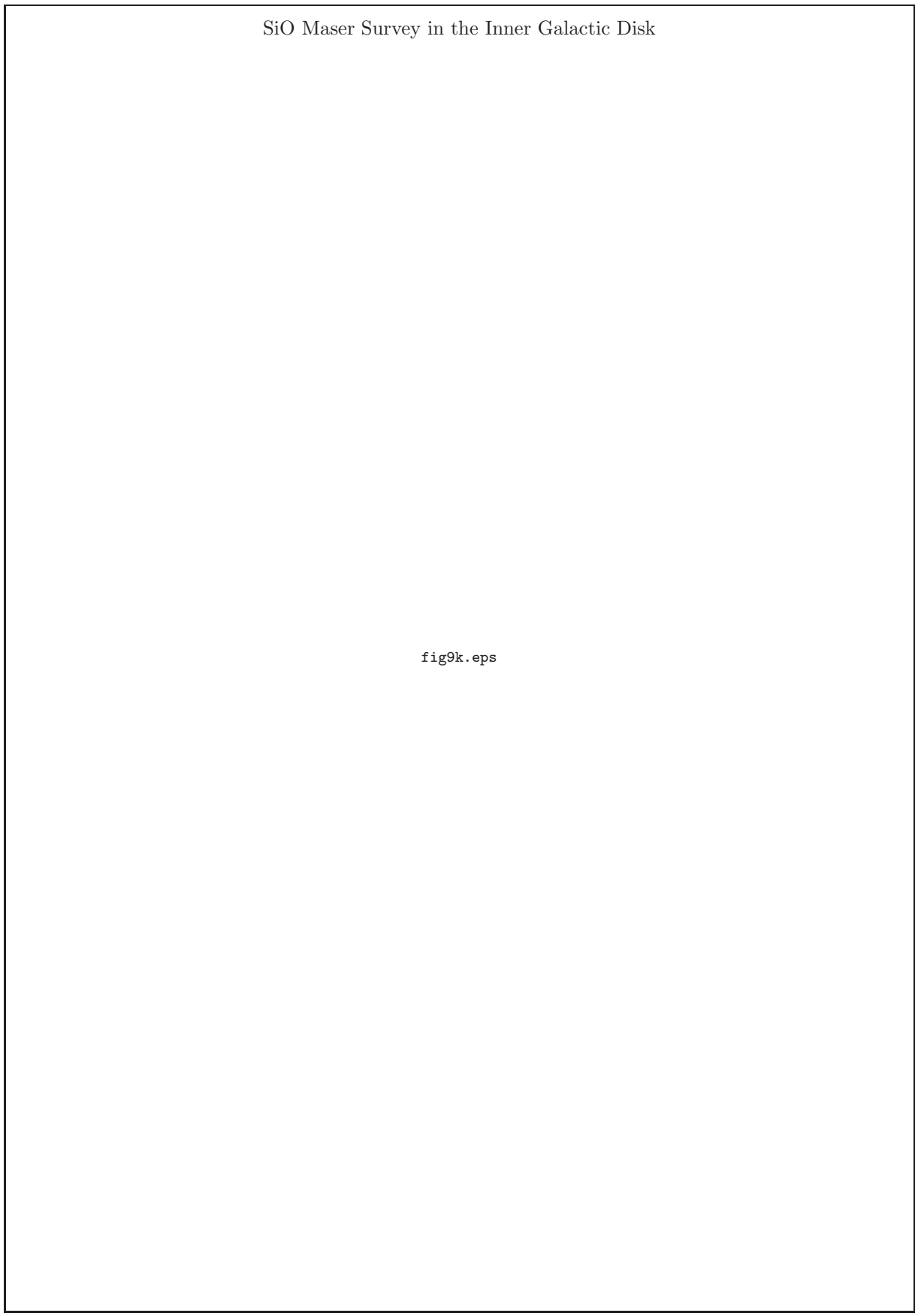

Fig. 9. k.

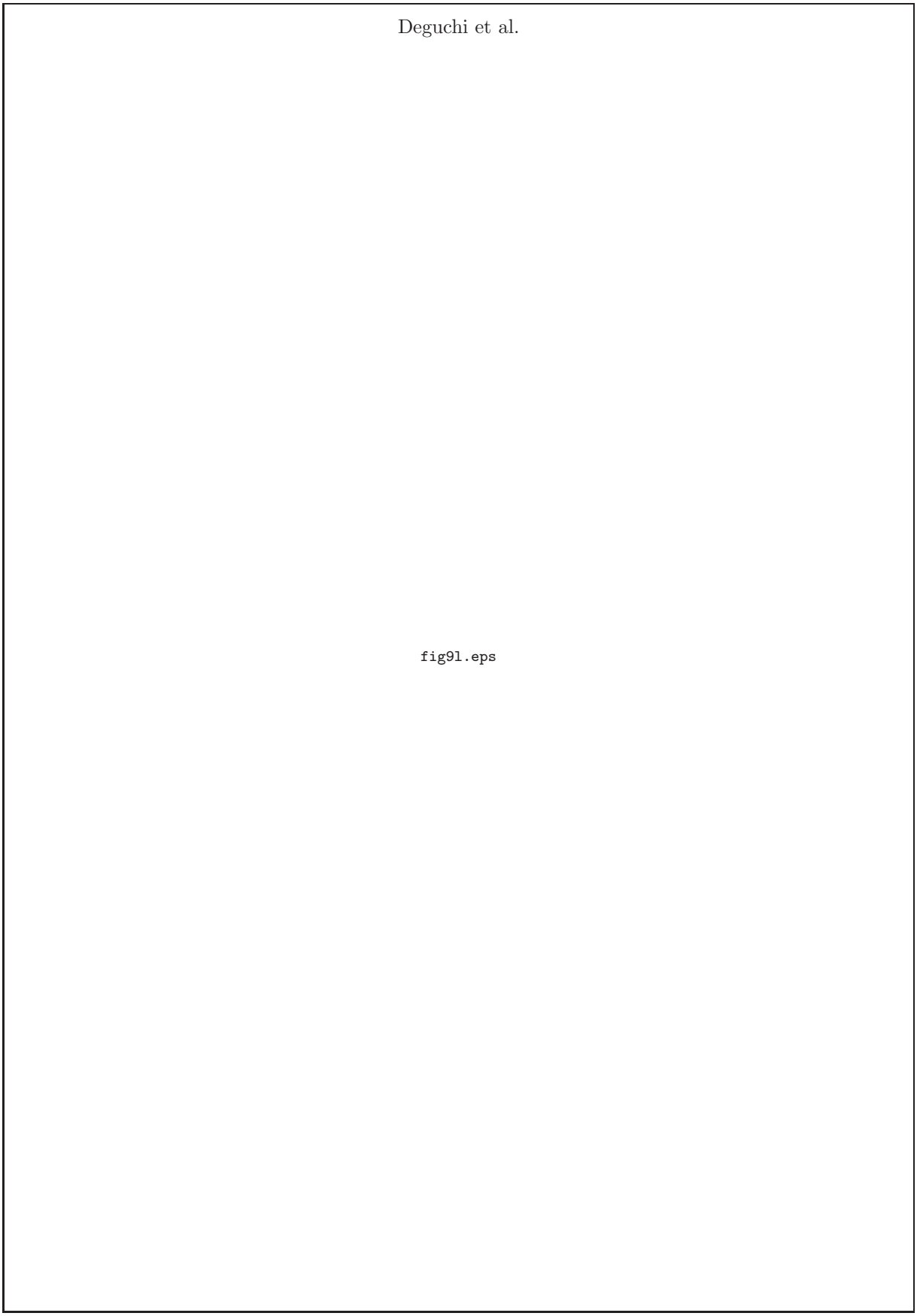

Fig. 9. l.

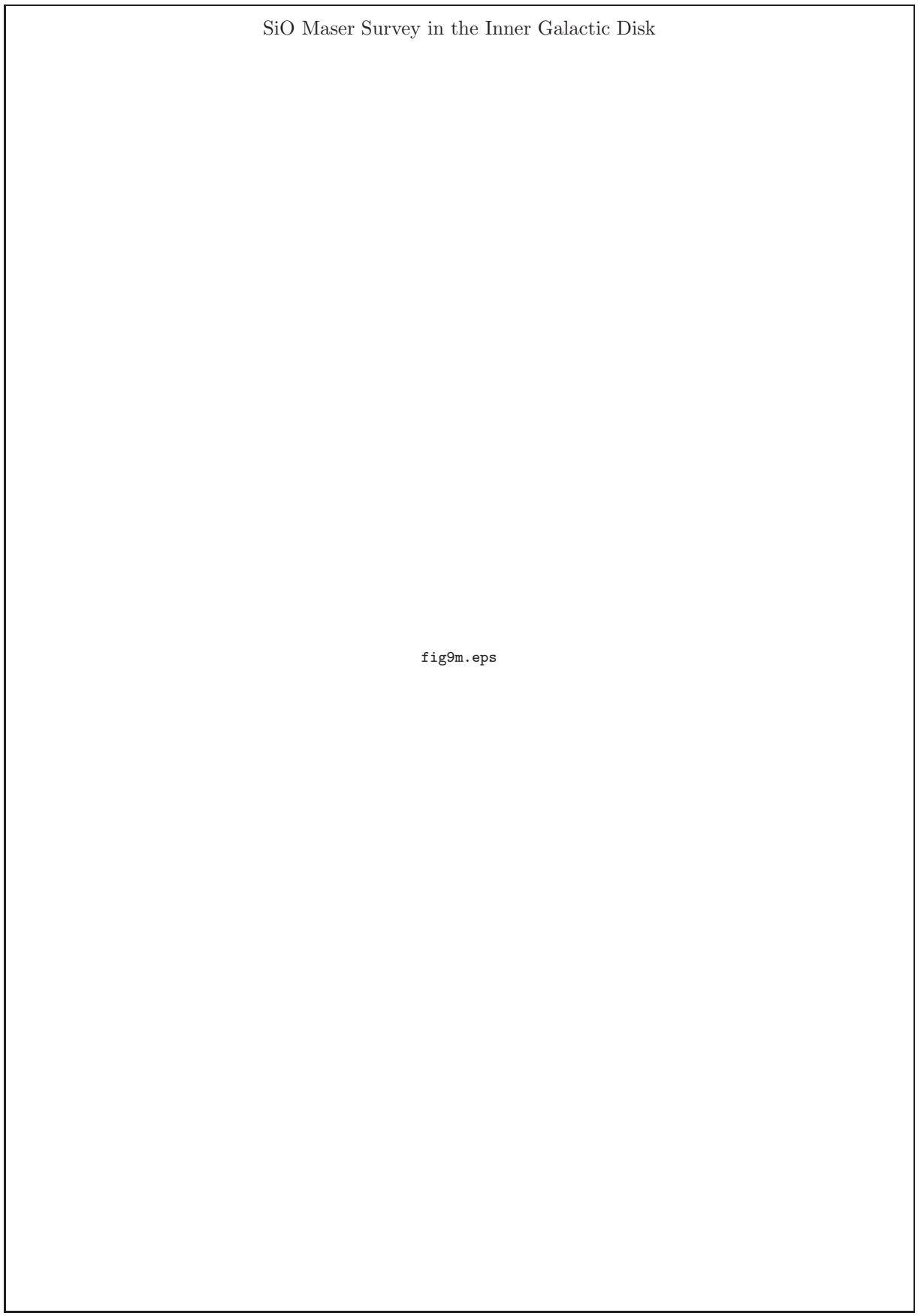

Fig. 9. m.

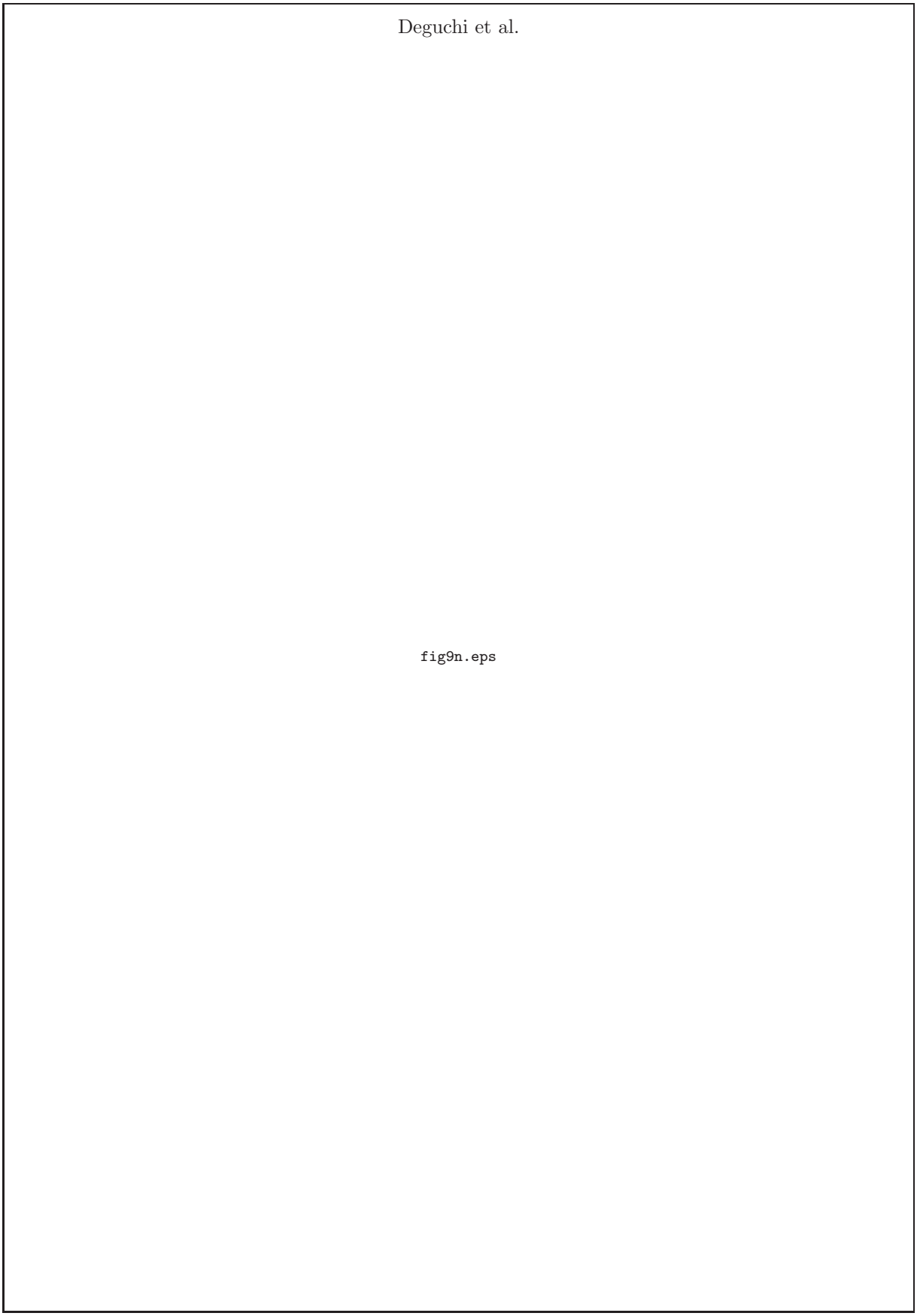

Fig. 9. n.

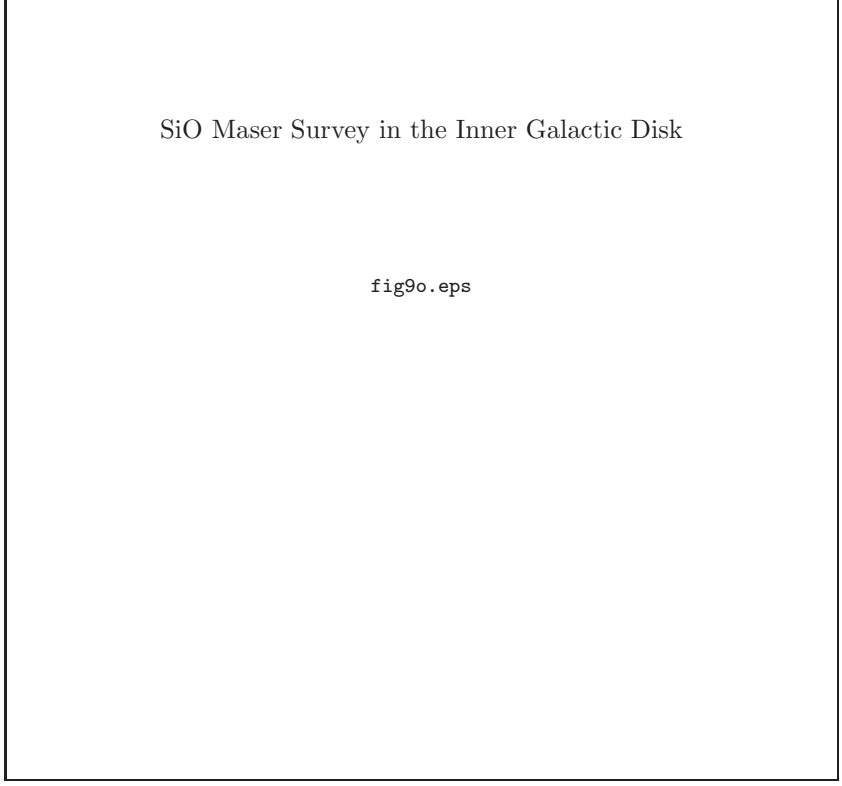

Fig. 9. o.

This figure "fig4.jpg" is available in "jpg" format from:
http://arXiv.org/ps/astro-ph/0407419v1

This figure "fig6.jpg" is available in "jpg" format from:

http://arXiv.org/ps/astro-ph/0407419v1

This figure "fig9a.jpg" is available in "jpg" format from:
http://arXiv.org/ps/astro-ph/0407419v1

This figure "fig9b.jpg" is available in "jpg" format from:

http://arXiv.org/ps/astro-ph/0407419v1

This figure "fig9c.jpg" is available in "jpg" format from:

http://arXiv.org/ps/astro-ph/0407419v1